ORIENTATION EFFECTS IN NANOCOMPOSITE FILMS AND GELS

by

JUN LI

A dissertation submitted to the Graduate Faculty in Physics in partial fulfillment of the requirements for the degree of Doctor of Philosophy

The City University of New York

2007

UMI Number: 3288741

ProQuest Information and Learning Company
300 North Zeeb Road
P.O. Box 1346
Ann Arbor, MI 48106-1346

This Manuscript has been read and accepted for the
Graduate Faculty in Physics in satisfaction of the
dissertation requirement for the degree of Doctor of Philosophy.

Steven A. Schwarz

_____

_____ _____

Date Chair of Examining Committee

Sultan Catto

_____

_____ _____

Date Executive Officer

Alexander Lisyansky

_____

Miriam Rafailovich

_____

Jonathan Sokolov

_____

Nan-Loh Yang

_____

Supervisory Committee

THE CITY UNIVERSITY OF NEW YORK

CITY UNIVERSITY OF NEW YORK

ABSTRACT

ORIENTATION EFFECTS IN
NANOCOMPOSITE FILMS AND GELS

by Jun Li

Advisor: Professor Steven A. Schwarz

We have studied the orientation effect of high aspect ratio nanofillers on spin cast nanocomposite films and nanocomposite hydrogels.

In the spin cast nanocomposite films project, we have shown that spin-cast polystyrene (PS)/Cloisite 6A (clay) nanocomposite films display a large radial thickness dependence that increases with clay concentration. Transmission electron microscopy reveals a tendency for the high aspect ratio clay particles to align in the direction of shear. Near the center of rotation, particles remain randomly oriented, leading to the formation of voids as the film dries. Atomic force microscopy shows that the roughness near the spin axis is higher than the roughness in the outer region. This proves that the orientation of clay platelets has a strong effect on the structure and thickness of films. A two dimensional numerical model that incorporates both hydrodynamic and orientation effects provides a good fit over a wide range of filler concentrations and spin rates.

In the nanocomposite hydrogels projects, we applied Small Angle Neutron Scattering (SANS) to study the shear induced clay orientation in Poly(ethylene oxide) (PEO)/ Laponite RD nanocomposite hydrogels. Under shear, the clay platelets may orient along the shear flow direction and may stretch the polymer chains bridging different clay platelets. The structure of the gel will turn from isotropic to anisotropic, therefore yielding anisotropic SANS

patterns. The experiments demonstrate that the evolution of the anisotropic SANS patterns depends on the temperature of the sample, concentration of PEO and clay, and the molecular weight. A two correlation length Debye-Anderson-Brumberger (DAB) model was applied to fit the SANS data. The short range correlation length is ~5 nm, which is likely to be the thickness of a domain composed of a clay platelet and the polymer chain wrapping it. While the long range correlation length is ~50 nm, which is similar to the distance between clay platelets. Under shear, clay platelets orient and polymer chains may be stretched; thus the both the long range and short rang correlation length will change. The correlation length along shear flow direction is observed to respond differently from that along the perpendicular direction.

TABLE OF CONTENTS

LIST OF FIGURES III

LIST OF TABLES VIII

ACKNOWLEDGEMENTS XI

CHAPTER 1 1

INTRODUCTION……...1

1.1 NANOFILLERS AND NANOCOMPOSITE...……..…..……..……...1

1.1.1 Noparticle...…..……..……..1

1.1.2 Nanotube, nanofiber, and nanorod…….....…….....5

1.1.3 Clay and nanocomposite……..….. ……..……...9

1.2 INTRODUCTION OF EXPERIMENTAL FACILITIES……...……15

1.2.1 TA ARES rheometer...…….……16

1.2.2 Small Angle Neutron Scattering (SANS)……..……...18

1.3 THESIS STRUCTURE ……...……....…….....21

CHAPTER 2……...……25

EFFECT OF CLAY PLATELET ORIENTATION ON SPIN CAST NANOCOMPOSITE FILMS……...25

2.1 INTRODUCTION……...……..25

2.2 EXPERIMENT……...……...……26

2.3 MODEL……..……..……30

2.4 CONCLUSION……...……...……34

CHAPTER 3……...……35

STRUCTURE AND THICKNESS MODELING FOR SPUN CAST POLYSTYRENE/CLAY NANOCOMPOSITE FILMS……35

3.1 INTRODUCTION...……...……...35

3.2 EXPERIMENTS……...……...……..37

3.2.1 Thickness of spin cast PS/clay toluene films……..37

3.2.2 TEM cross section……39

3.2.3 Atomic force micrographs (AFM) of a Langmuir-Blodgett cloisite 6A film……..41

3.2.4 Viscosity…...……42

3.2.5 Evaporation rate……..……46

3.3 MODEL……...…49

3.3.1 Mass transfer model……...…….50
3.3.2 Amendment of the mass transfer model to include an orientation effect…...……...…….54
3.4 SIMULATION RESULT AND DISCUSSION……...……...….57
3.5 CONCLUSION……...……...……59

CHAPTER 4……..61
EFFECT OF TEMPERATURE ON SHEAR INDUCED ANISOTROPIC STRUCTURE IN POLYMER CLAY HYDROGELS……...61
4.1 INTRODUCTION……...……...……61
4.2 EXPERIMENT……...……...……63
4.3 RESULTS AND ANALYSIS……...64
4.4 CONCLUSION……...……...…….71

CHAPTER 5……..73
SHEAR RESPONSE IN POLYMER CLAY NANOCOMPOSITE HYDROGELS……...73
5.1 INTRODUCTION……...……...……...……...73
5.2 EXPERIMENTS……...……...……...75
5.3 RESULTS AND ANALYSIS…….....……76
5.4 CONCLUSION……...…...……..87

CHAPTER 6……..89
SUMMARY……...89

BIBLIGRAPHY……92

LIST OF FIGURES

Number *Page*

Fig. 1-1. Computer graphic showing a nanotube composed of two helicoidal shells. 5

Fig. 1-2. Structure of 2:1 phyllosilicates. [63,64] 10

Fig. 1-3. Scheme of different types of composite arising from the interaction of layered silicates and polymers: (a) phase-separated microcomposite; (b) intercalated nanocomposite and (c) exfoliated nanocomposite.[1] 12

Fig. 1-4 A picture of the TA ARES rheometer. 16

Fig. 2-1. A nanocomposite flm spun cast on silicon at 3000 rpm for 30 s from a solution of PS (60mg/ml)/Cloisite 6A (30mg/ml)/toluene. The film thickness is ~ 4 μm in the center, decreasing to ~ 4 μm at the periphery. a) Photograph (Nikon Coolpix 4500) of the film. b) confocal microscope image (Leica TCS SP2) of the central region as indicated. 26

Fig. 2-2. PS/clay/toluene spin cast films. The symbols represent measured data. The dash lines are the prediction of the mass transfer model. The solid lines are predicted by the orientation model. (a) spin rate 2000 rpm, PS 60 mg/ml, clay concentrations as indicated. (b) PS 60 mg/ml, clay 30 mg/ml, spin rates as indicated. 27

Fig. 2-3. Cross section TEM images of PS (60 mg/ml)/clay (40 mg/ml) spun cast films on vinyl cyclohexene substrate (a) center region, and (b) outer region. 28

Fig 2-4. AFM topographical images of polymer films spun cast at 2000 rpm. (a) PS film without clay, (b) the outer region of a PS (60 mg/ml)/clay (10 mg/ml) film, and (c) the center region of the same PS/clay film. 29

Fig. 3-1. The effect of clay concentration on the thickness distribution for PS/clay/toluene spin cast films, PS concentration is 60mg/ml and clay concentrations vary as indicated. The spin rate was 2000 rpm, spin time was 60 s, and the treated silicon wafers were hydrophobic. 38

Fig. 3-2. The effect of spin rate on the thickness distribution for PS/clay/toluene spun cast films on as received silicon wafers for a PS concentration of 60 mg/ml and clay concentration of 40 mg/ml . The spin time is 30 s, spin rates vary as indicated. 39

FIG. 3-3. Cross Section TEM pictures for PS/clay spin cast films on vinyl cyclohexene substrates with a PS concentration of 60 mg/ml, clay concentration of 40 mg/ml, spin rate of 3000 rpm, and spin time of 30 s. (a) Cross-section cut from the center region along a radial direction. (b) Cross-section cut from the center region along a tangential direction. (c) Cross-section cut from the outer region along a radial direction. (d) Cross-section cut from the outer region along a tangential direction. 40

FIG. 3-4. AFM micrograph of a Cloisite 6A Langmuir-Blodgett(LB) film deposited on a silicon substrate. The line indicates a platelet dimension of 473 nm. 42

Fig. 3-5. Viscosity of PS/toluene solutions as a function of shear rate, were measured by a TA ARES rheometer in the cone plate geometry. The numbers

represent the PS concentration of each sample in units of mg/ml. The solid lines indicate the magnitudes predicted by Eq. (2). 43

Fig. 3-6. Viscosity of PS/clay/toluene solutions as a function of shear rate. The PS concentration is 60 mg/ml, while the clay concentration varies as indicated. The solid lines are plots of Eq. (3.1). 44

Fig. 3-7. Viscosity of PS/clay/toluene solution for PS/clay concentration ratios of 3/2. The numbers represent the PS concentration/ clay concentration of the sample in units of mg/ml. The solid lines are plots of Eq. (3.1). 45

Fig. 3-8. The normalized evaporation rate, y, determined by mass loss measurement, is plotted as a function of (spin rate/100 rpm)$^{1/2}$, x. The linear fit is given by $y = 1.12\,x - 0.17$. 48

Fig. 3-9. Evaporation rate ratio vs PS concentration, as determined by mass loss measurements, PS/clay concentration ratios vary as indicated. 49

Fig. 3-10. Normalized film thickness vs. radius for spun cast PS/clay/toluene films on as received silicon wafer. PS concentration is 60 mg/ml, clay concentration is 40mg/ml, spin rate is 2000 rpm, spin time is 30s. (a) Measured data. (b) Model predictions including the effect of platelet orientation. (c) Model predictions without including the effect of orientation, and with a magnified view in the inset. 58

Fig. 4-1. Two dimensional SANS scattering patterns at three temperatures, with shear rates (s^{-1}). The patterns at the far right were obtained immediately after the application of highest shear, with the Couette cell at rest. 64

Fig. 4-2. a) SANS anisotropy |(Iy- Ix)/(Iy+Ix)| as a function of shear rate and q at 2°C b) Anisotropy averaged over the entire q range as a function of shear rate at three different temperatures as indicated. 65

Fig. 4-3. Static SANS intensity vs. q at 10°C and 40°C. Solid lines show the fits obtained by the DAB model for the parameters given in Table 4-1. 67

Fig. 4-4. Application of the DAB model to the dynamic SANS data averaged over a 10° range in the X (parallel) and Y (perpendicular) directions. a) and b): Short range correlation lengths parallel and perpendicular to the shear flow direction; c) and d): Corresponding long range correlation lengths; e) and f): Corresponding relative strengths of long range correlation $1-f$. 70

FIG.5-1. Two dimensional SANS scattering patterns for five samples under different shear rates (s^{-1}) as indicated above. a) LP1, b) LP4, c) LP6, d) LP7, e) LP8. 77

Fig. 5-2 Shear dependence of average SANS anisotropy $|(I_y-I_x)/(I_y+I_x)|$ over entire q range. 79

Fig. 5-3 SANS intensity curves for sample LP4 under shear rate 400 s^{-1}; averaged data along X and Y direction in a range of 10°. Solid lines represent the prediction from the two correlation DAB model. 80

Fig. 5-4 Fits of the circular average intensity data at 0 shear rate with DAB model show an R1 dependence on polymer/clay volume ratio. 82

Fig. 5-5 Fits of the section average intensity data at different shear rates along X and Y directions, a) R1 dependence on shear rate; b) R2 dependence on shear rate. 83

Fig. 5-6 Corresponding fit result along X and Y direction of relative weight of long range correlation, 1-f , dependence on shear rate. 84

Fig. 5-7 Frequency response a) Elastic modulas, G'; b)Loss modulas, G". 86

LIST OF TABLES

Number *Page*

Table 4-1. DAB fitting results for static SANS data 68

Table 5-1 Sample wt. concentration (%) 75

ACKNOWLEDGMENTS

The author wishes to thank all the professors for their guidance through the six years' studying, thank all the classmates for their cooperation, and thank all the friends for their encouragement and support.

First and foremost, I am deeply indebted to my supervisor, Prof. Steven A. Schwarz from Queens College of City University of New York. He always encourages me to seek after new ideas and technology, guides me through the research work, and helps me on my career development without any reservation. I will benefit from his profound knowledge and nice personality in all my life.

I would like to express my gratitude to Prof. Miriam Rafailovich and Prof. Jonathan Sokolov for their direction on my research work and their help on my career development. I also would like to thank Prof. Alexander Lisyansky, Prof. Nan-Loh Yang, Prof. A. Genack, Vladimir Zaitsev, Donna Hernandez, Bob Bunch, Grigory German, and Howard Rose for their great help during these several years' study, A special thanks goes to Dr. Min Yue Lin for his direction and kind assistance on the neutron scattering experiment.

I appreciate the cooperation from my classmates and friends from SUNY Stony Brook; they are Mayu Si, Xuesong Hu, Bingquan Li, Yuan Ji, Yantian Wang, Yuan Sun, Jun Jiang, Chunhua Li, Xiaohua Fang, Song Li, Shouren Ge, Wentao Li, Haobin Luo. I also appreciate the valuable discussion and strong support from my friends: Li Chen, Bing Hu, Ke Tang, Huafeng Xie, Xiaowei Xu , Jing Wang, Sean Zhang, Sheng Zhang, Kungang Zhou.

Lastly, I am grateful to my mother, Yuebing Yang, for her encouragement and support on my studies during the past several years. My two brothers, Wei Li and Bo Li spent a lot of time and energy to take care of our mom, therefore I can concentrate on my study; I really appreciate their contribution. Since my father has passed away a long time ago, he always lives in my heart and this thesis is in memory of my deeply loved father, Changyou Li.

Chapter 1

INTRODUCTION

1.1 Nanofillers and nanocomposite

In recent years, nanocomposite materials have attracted a lot of attention in academic research and industry application. Nanocomposites are particle-filled polymers for which at least one dimension of the dispersed particles is in the nanometer range. There are three types of nanocomposites, depending on how many dimensions of the dispersed particles are in the nanometer range. When the three dimensions are on the order of nanometers, we are dealing with isodimensional nanoparticles, such as spherical silica nanoparticles, semiconductor nanoclusters, gold nanoparticles, and silver nanoparticles. When two dimensions are in the nanometer scale and the third is larger, an elongated structure like nanotubes or whiskers is formed. Currently, carbon nanotubes or cellulose whiskers are extensively studied as reinforcing nanofillers yielding materials with exceptional properties. The third type of nanocomposites only has one dimension in the nanometer range. In this case the filler is present in the form of sheets with thickness range from one to a few nanometers, while the length may be hundreds to thousands of nanometers long. These materials are obtained by the intercalation of the polymer (or a monomer subsequently polymerized) inside the galleries of layered host crystals. There is a wide variety of both synthetic and natural crystalline fillers that are able to intercalate a polymer under some specific conditions.[1]

1.1.1 Nanoparticles

Nanoparticles have become a most exciting area of research in recent years. So far a lot of metal nanoparticles, alloy nanoparticles, metal compound nanoparticles, and organic nanoparticles have been synthesized, and these nanoparticles have been introduced into different materials to improve certain properties.

Metal nanoparticles play important roles in many different areas. The intrinsic properties of a metal nanoparticle are mainly determined by its size, shape, composition, crystallinity, and structure (solid versus hollow). In principle, one could control any one of these parameters to fine-tune the properties of this nanoparticle. Controlling the size, shape, and structure of metal nanoparticles is technologically important because of the strong correlation between these parameters and optical, electrical, and catalytic properties. Gold nanoparticles are very popular; they have been applied extensively to make devices. Other metal metals particles, such as silver, cobalt, gallium, and dysprosium nanoparticles have also attracted much interest because of their special properties.

Sun and Xia have synthesized silver nanocubes in large quantities by reducing silver nitrate with ethylene glycol in the presence of poly(vinylpyrrolidone) (PVP). They further used silver cubes as sacrificial templates to generate single-crystalline nanoboxes of gold.[2] A single gold nanoparticle can act as a nanoantenna in the near field of a sample and the modification of its intrinsic radiative properties by monitoring its plasmon spectrum has been studied.[3] Effective utilization of coupled surface plasmon resonance from gold nanoparticles has been demonstrated experimentally for optoelectronic applications based on second-order nonlinear optics; the second harmonic light intensity was enhanced by a factor of 8.[4] Schaadt and

coworkers have engineered enhancement of optical absorption and photocurrent in a semiconductor via the excitation of surface plasmon resonances in spherical gold nanoparticles deposited on the semiconductor surface.[5] Introduction of gold nanoparticles into poly(9,9'-dioctylfluorene) can make nanocomposite Light-Emitting Diodes and has enhanced the electroluminescence stability and quantum efficiency of Blue-Light-Emitting Polymers.[6] Gittins and coworkers have showed that organic molecules containing redox centres can be used to attach gold nanoparticles to electrode surfaces and so control the electron transport between them; they expected this to form the basis for a range of nanoscale electronic switches.[7] The application of other metal nanoparticles have also been extensively studied. Silver nanoparticles have been applied to make dipole nanolasers;[8] memory effect has been observed in cobalt nanoparticle systems;[9] optical nonlinearity resulting from a light-induced structural transition in gallium nanoparticles has been demonstrated;[10] embedding dysprosium nanoparticle into a sputtered film matrix leads to special magnetic property related to the particle size.[11]

Compared to metal nanoparticles, some alloy nanoparticles may have stronger magnetic properties. Sun and coworkers have synthesized monodisperse iron-platinum (FePt) nanoparticles by reduction of platinum acetylacetonate, and decomposition of iron pentacarbonyl in the presence of oleic acid and oleyl amine stabilizers is reported.[12] They further produced exchange-coupled isotropic FePt–Fe3Pt nanocomposites with an energy product of 20.1 MGOe, which exceeds the theoretical limit of 13 MGOe for nonexchange-coupled isotropic FePt by over 50 per cent.[13] Cobalt platinum alloy, Co_xPt_{100-x}, nanoparticles with dimensions from approximately 2 to 5 nm can be synthesized using the reverse micelle method. Composition atomic ratio of Co to Pt at around unity gives the highest coercivity of 5500 Oe at

room temperature.[14] Samarium cobalt alloy nanoparticles, and iron cobalt alloy nanoparticles also showed the super-paramagnetic property.[15]

Metal compound nanoparticles have also been extensively applied in different areas. It has been reported that vanadium dioxide nanoparticles can dramatically enhance the optical contrast between the semiconducting and metallic phases in the visible region;[16] $CoRh_2O_4$ nanoparticles show a systematic magnetic enhancement below T_N.[17] The magnetic properties of NiH_x nanoparticles are quite different from those of Ni nanoparticles, and they have been considered to be important materials that can be used for hydrogen storage for both fuel cells and electrodes in batteries.[18] Nanoparticles of indium oxide, synthesized by pulsed laser ablation of a pure indium metal target, have a band gap close to GaN[19]; nanoparticle crystalline iron phosphates ($FePO_4 \cdot 2H_2O$ and $FePO_4$) were synthesized using a (CTAB) surfactant as an anode material for Li rechargeable batteries.[20] Sun and coworkers have showed that photovoltaic devices fabricated from blends of branched CdSe nanoparticles and a conjugated polymer give improved performance compared with devices made from nanorod/polymer blends.[21]

Now organic nanoparticles have also attracted a lot of interest. It has been reported that hyperbranched polymers (HBPs) act as mobile organic nanoparticles doped in methacrylate photopolymers for highly efficient volume holographic recording.[22] A new class of organic nanoparticles (CN-MBE nanoparticles) with a mean diameter of ca. 30- 40 nm, prepared by a simple reprecipitation method, exhibit a strongly enhanced fluorescence emission.[23] Organic nanoparticles have also been applied to fabricate memory devices, which exhibit nonvolatile memory characteristics at low operation

voltages and do not show any change of characteristics with time in normal ambient conditions .[24]

1.1.2 Nanotube, nanofiber, and nanorod

For nanotube, nanofiber and nanorod, only two dimensional sizes are in the nanometer scale, the size in the other dimension is much bigger. Thus the aspect ratio for these fillers is very big. Specific sizes and properties of these fillers have been the subject of extensive research and application. In particular, carbon nanotubes have been a scientific frontier since 1990.

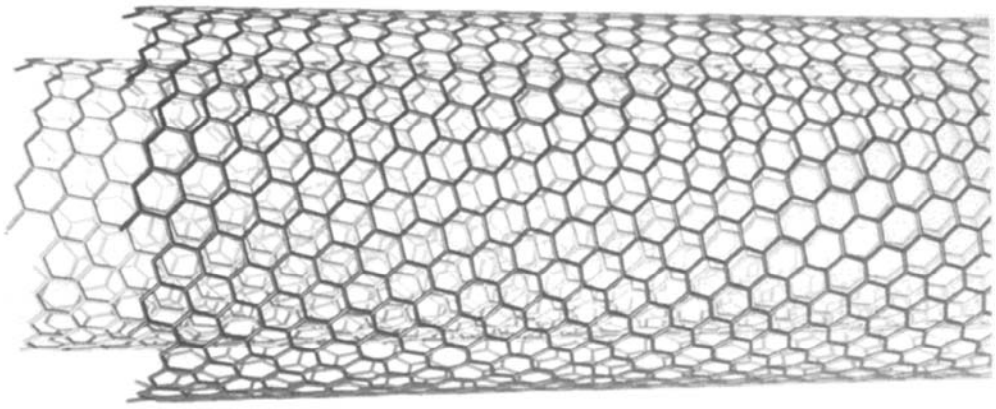

Fig. 1-1. Computer graphic showing a nanotube composed of two helicoidal shells.[25]

A carbon nanotube is a seamless cylindrical sheet of graphite whose diameter is so small and its aspect ratio is so great that it can be considered from the electronic point of view as a one-dimensional structure. In the absence of external strain, a carbon nanotube is always straight unless carbon

rings having a number of carbons different from six (pentagons, heptagons, octagons, etc.) are present in the hexagonal network. A nanotube may consist of one or more cylindrical shells of graphitic sheets (sometimes called graphene) as shown in Fig. 1-1.[25] The exact structure of the carbon nanotube depends on the methods of preparation. The fabrication methods of nanotubes have been developed since 1990. There are mainly three ways to fabricate carbon nanotubes, which are: carbon arc, carbon vapor deposition, and catalytic methods. The outer diameter varies typically between 2 and 20 nm in the arc-produced nanotubes, while the inner hollow diameter is typically on the order of 1 to 3 nm.[26] The single shell nanotubes produced with catalysts have a much narrower distribution centered around 1.2 nm.[27-28] In multilayered nanotubes, the interlayer distance is ~ 0.34 nm, which corresponds to the interlayer distance in graphite. The arrangement of the carbon atoms in the hexagonal network of the tube is more often than not helicoidal, which results in chiral tubes.[29]

In recent years, the application of carbon nanotubes has developed fast in many different areas. Field-effect transistors have been fabricated based on individual single- and multi-wall carbon nanotubes[30-33]; they have even been applied to make a logic circuit.[34-35] Carbon nanotubes have also been applied to fabricate a field-emission flat panel display; further improvement of this technology may lead to easy-to-make and inexpensive flat panel displays.[36-37] The unique chemical and physical properties of carbon nanotubes also paved the way to new and improved sensing devices in general, and electrochemical biosensors in particular. Upon exposure to gaseous molecules such as NO_2 or NH_3, the electrical resistance of a semiconducting single wall nanotube is found to dramatically increase or decrease, and this serves as the basis for nanotube molecular sensors.[38] Carbon nanotube based electrochemical

transducers offer substantial improvements in the performance of amperometric enzyme electrodes, immunosensors and nucleic-acid sensing devices.[39] A gas can be condensed to high density inside the narrow single wall nanotubes and therefore make them effective hydrogen storage materials for fuel cell electrical vehicles.[40] Carbon nanotubule membranes can also be filled with nanoparticles of electrocatalytic metals and alloys to be used to electrocatalyse oxygen reduction and methanol oxidation, two reactions of importance to fuel-cell technology.[41] The high stiffness and strength, low density, and large aspect ratio of single-walled carbon nanotubes make them good candidates as ultrahigh frequency nanomechanical resonators.[42] Electromechanical actuators based on sheets of single-walled carbon nanotubes were shown to generate higher stresses than natural muscle and higher strains than high-modulus ferroelectrics.[43] We can even dope carbon nanotubes with some specific material to improve certain properties, for example, the magnetic property can be improved by doping cobalt,[44] and the conductivity can be enhanced by doping potassium (K) and bromine (Br).[45] Carbon nanotube transistors will exhibit high on-state conductance, carrier mobilities, and on-off ratios by doping polymer electrolytes.[46]

Nanofibers have a shape similar to nanotubes, but they are relatively longer and may not be hollow. Metal nanofibers can be fabricated by using the gas-evaporation method in the presence of electric fields[47]; polymer nanofibers can be made by electrospinning.[48-50] Now nanofibers have been applied to a lot of different areas. A non-woven poly(ε -caprolactone) (PCL) scaffold made by electrostatic fiber spinning can be used for bone tissue engineering. Poly(L-lactide-*co*-ε-caprolactone) [P(LLA-CL)] nanofiber may be a biomimetic extracellular matrix for smooth muscle cell and endothelial cell proliferation.[50] The addition of carbon nanofiber to polypropylene can lead to a 350% increase

of dynamic modulus while still maintaining similar thermal behavior. [51] A Pt-Ru/graphitic carbon nanofiber nanocomposite exhibits high relative performance as a direct-methanol fuel cell anode catalyst.[52] Doping a zinc oxide nanofiber array with gallium can improve electric properties of nanofibers and enhance field emission.[53] It was found that not only the activity but also the selectivity of nickel crystallites could be dramatically altered when using graphite nanofiber to supported nickel particles as catalyst.[54] Polyaniline Nanofiber Gas Sensors perform better than conventional thin films because their high surface area, porosity and small diameters enhance diffusion of molecules and dopants into the nanofibers.[55] Vanadium oxides (V_2O_5) nanofiber actuators provide the potential advantages of low-cost synthesis by sol-gel routes and high charging capacity and long cycle life.[56]

The length of nanorods are usually smaller than that of nanotubes and nanofibers, but their aspect ratios are still big. The shape and size of nanorods may vary with respect to fabrication method and conditions. The synthesis of Barium Titanate (BaTiO3) and Strontium Titanate (SrTiO3) nanorods can be accomplished by solution-phase decomposition of bimetallic alkoxide precursors in the presence of coordinating ligands.[57]. The CdS nanorod can be fabricated by using a monosurfactant system under atmospheric benchtop conditions.[58] Gold and silver nanorods of diameter 40 and 90 nm and having a variety of aspect ratios (length/diameter) can be prepared using the template synthesis approach.[59] Recently the application of nanorods has also aroused a lot of interest. Composites of inorganic nanorods and a conjugated polymer have been used to make photovoltaic cells.[60] Dislocation-free indium gallium nitride/gallium nitride multiquantum-well nanorod arrays can improve the total external efficiency and brightness of light emitting diodes.[61] Semiconductor

nanorods can be used to fabricate readily processed and efficient hybrid solar cells together with polymers.[62]

1.1.3 Clay and nanocomposite

Recently clay has also been a popular filler because it can be used to make nanocomposite materials at low cost. Under certain conditions, clay can exfoliate into platelets with the thickness at ~1nm, but the lateral size can be much bigger. Usually the aspect ratio of clay platelet is very big, and the orientation of clay platelets is important to the structure and property of the material.

Clays or layered silicates are a subgroup of the general class of layered solids that includes such materials as graphite intercalation compounds, layered perovskites, and layer dichalcogenides. Most rigid clays have a 2:1-layered silicates structure as shown in Fig.1-2; [63-65] they can also have a 1:1 layer type and a 2:1 inverted ribbon structure [66]. In 2:1-layered silicate structure, central to the tetrahedral layers are silicon or aluminum (Al) ions, which are tetrahedrally bonded to oxygens. The number of A1 ions in tetrahedral sites determines the net negative charge of the host layer. Those oxygens forming the tetrahedral bases border the interlamellar gallery and are arranged in hexagonal rings that form a kagomé lattice. At the geometric mid-plane of each clay layer resides an atom octahedrally coordinated to those oxygens comprising the tetrahedron tip. The layer thickness is around 1 nm and the lateral dimensions of these layers may vary from 300 Å to several microns and even larger depending on the particular silicate. These layers organize themselves to form stacks with a regular van der Waals gap in between them called the interlayer or the gallery. Isomorphic substitution within the layers (for example, Al^{3+} replaced by Mg^{2+} or by Fe^{2+}, or Mg^{2+}

replaced by Li^+) generates negative charges that are counterbalanced by alkali or alkaline earth cations situated in the interlayer. The net negative charge on the host layer component of each unit cell is 0 or $1e^-$; thus 2:1 clays are anionic. This charge is balanced within the unit cell by the charge on the gallery cation. In the simplest picture, this cation nests below and above the hexagonal cavities and is surrounded by six basal oxygens and the hydroxyl group of each layer. As the forces that hold the stacks together are relatively weak, the intercalation of small molecules between the layers is easy. [1,63]

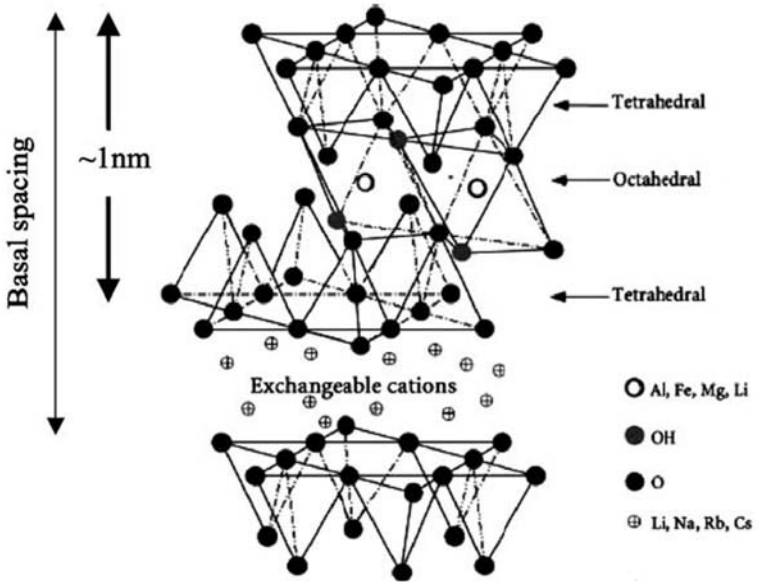

Fig. 1-2. Structure of 2:1 phyllosilicates. [63, 64]

Introducing clay to polymer, we can make a polymer clay composite with the structure depending on the nature of the components used (layered silicate, organic cation and polymer matrix) and the method of preparation. As shown in Fig. 1-3, generally there are three types of composite: microcomposites, intercalated nanocomposites, and exfoliated nanocomposites. When the

polymer is unable to intercalate between the silicate sheets, a phase separated composite (a) is obtained, whose properties stay in the same range as traditional microcomposites. Beyond this classical family of composites, two types of nanocomposites can be recovered. The first is an intercalated structure (b) in which a single (and sometimes more than one) extended polymer chain is intercalated between the silicate layers resulting in a well ordered multilayer morphology built up with alternating polymeric and inorganic layers. Second, when the silicate layers are completely and uniformly dispersed in a continuous polymer matrix, an exfoliated or delaminated structure is obtained (c).[1] Ray and Okamoto pointed out there is another kind of nanocomposite, flocculated nanocomposites, which conceptually are the same as intercalated nanocomposites but silicate layers are sometimes flocculated due to hydroxylated edge–edge interaction of the silicate layers.[65]

The large variety of polymer systems used in nanocomposites preparation with layered silicate can be conventionally classified as: vinyl polymers, condensation (step) polymers, polyolefins, biodegradable polymers, and specialty polymers like poly(N-vinylcarbazole) (PNVC) and polyaromatics such as polyaniline (PANI). [65-67] Polymer clay nanocomposites can be prepared by several methods: exfoliation/adsorption, chemical/thermal conversion, in situ intercalative polymerization, melt intercalation and template synthesis.[67]

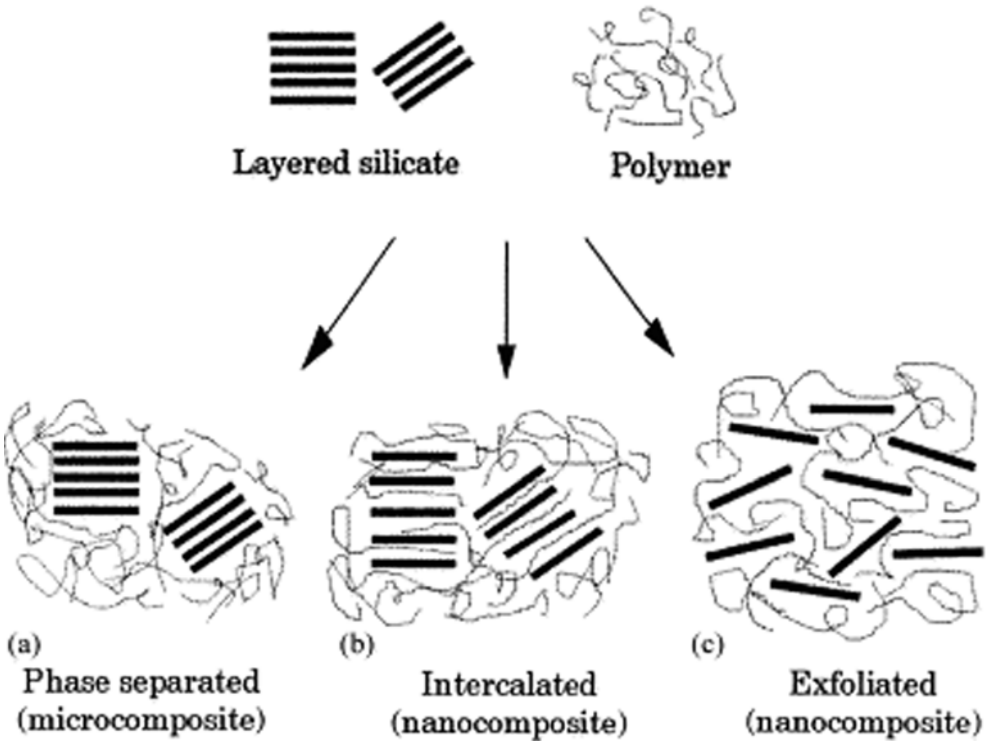

Fig. 1-3. Scheme of different types of composite arising from the interaction of layered silicates and polymers: (a) phase-separated microcomposite; (b) intercalated nanocomposite and (c) exfoliated nanocomposite.[1]

_ Exfoliation/adsorption: The layered silicate can be exfoliated into single layers using a solvent in which the polymer is soluble. As the forces that stack the layers together are weak, clay will be dispersed in an adequate solvent. The polymer then adsorbs onto the delaminated sheets and when the solvent is evaporated (or the mixture precipitated), the sheets reassemble, sandwiching the polymer to form, in the best case, an ordered multilayer structure. Under this process are also gathered the nanocomposites obtained through emulsion polymerization where the layered silicate is dispersed in the aqueous phase.

_ In situ intercalative polymerization: The layered silicate is swollen within the liquid monomer (or a monomer solution) so that the polymer formation can occur in between the intercalated sheets. Polymerization can be initiated either by heat or radiation, by the diffusion of a suitable initiator or by an organic initiator or catalyst fixed through cationic exchange inside the interlayer before the swelling step by the monomer.

_ Melt intercalation: The layered silicate is mixed with the polymer matrix in the molten state. Under these conditions and if the layer surfaces are sufficiently compatible with the chosen polymer, the polymer can crawl into the interlayer space and form either an intercalated or an exfoliated nanocomposite. In this technique, no solvent is required.

_ Template synthesis: In this case, the silicates are formed in situ in an aqueous solution containing the polymer and the silicate building blocks. This has been widely used for the synthesis of double-layer hydroxide-based nanocomposites,[70-71] but is far less developed for layered silicates. In this technique, based on self-assembly forces, the polymer aids the nucleation and growth of the inorganic host crystals and gets trapped within the layers as they grow.[1]

Nanocomposites consisting of a polymer and clay (modified or not) frequently exhibit remarkably improved mechanical and materials properties because of the stronger interfacial interaction between the matrix and clay. Compared with conventional filler-reinforced systems, nanocomposite materials have a higher modulus, strength, and heat resistance, a lower decreased gas permeability and flammability, and a better biodegradability of biodegradable polymers. In systems consisting of poly(ε-caprolactone) and

nylon-6 with varying amounts of layered silicate (montmorillonite), the storage (G') and loss (G") moduli increase at all frequencies with increasing silicate loading.[72] For poly(ethylene oxide) (PEO)/organoclay nanocomposites prepared via a solvent casting method, a hysteresis phenomenon was also enhanced with organoclay content, and the increase in the storage/loss modulus and interactions among organoclay platelets were observed, as well as enhanced thermal stability .[73] The nanocomposite of PS and sodium ion-exchanged montmorillonite (Na+-MMT) exhibits more pronounced shear thinning behavior with increasing clay content.[74] In adhesive nanocomposites of organically modified montmorillonite (OM) and polyurethane, small volume fractions of the platelike nanoparticles in the polymer matrix decreased the transmission rate of oxygen and water vapor.[75] Montmorillonite (MMT) based nanocomposite systems show reduced flammability, and it has been show that the MMT must be nanodispersed for it to affect the flammability.[76] It has been reported that the introduction of Cloisite 30B to biodegradable aliphatic polyester will lead to a lower biodegradability.[77]

As polymer clay nanocomposite materials show some advantage over traditional polymer material, they have been applied widely. They are used to make tires, flexible and rigid packaging such as films, bottles, trays, and blister packs, and also for electronics plastics such as wire and cable coatings. Triphase catalytic materials based on alkylammonium exchange forms of smectite clays can be used as efficient, stable, and recyclable catalysts for a variety of organic chemical conversions.[78] A novel bentonite clay-based Fe-nanocomposite (Fe-B) was successfully developed as a heterogeneous catalyst for photo-Fenton discoloration and mineralization of an azodye Orange.[79] It has also been demonstrated that montmorillonite clay hybridized into liquid crystal yields many advantages to improve the electro-optical properties of a

display device.[80] The use of nanocomposites also constitutes a versatile and robust approach in the development of novel electrolytes with tailored electrochemical and mechanical characteristics.[81] Biopolymer-clay nanocomposites allow the development of electrochemical sensors for the potentiometric determination of anionic species, which shows a higher selectivity towards monovalent rather than to di- or trivalent anions and the best potentiometric response towards nitrate ions.[82]

1.2 Introduction of experimental facilities

The work shown in this thesis is mainly composed of research work on two projects: nanocomposite films and nanocomposite gels. In the project on nanocomposite films, a Dektak IIA surface profilometer was applied to measure film thickness at different locations on the wafer, a TA ARES rheometer was applied to measure the viscosity of Polystyrene(PS)/Cloisite 6A solutions, a Headway spinner was used to spin cast the nanocomposite film, and then a Leica TCS SP2 confocal microscope was applied to examine the surface shape. A JEOL JEM1200 TEM was used to obtain images of the cross-section of spun cast PS/Cloisite nanocomposite films, an Atomic Force Microscope (AFM) Dimension 3000 was applied to study the roughness of the films, and a KSV 5000 LB trough was used to make Langmuir-Blodgett Cloisite 6A films. In the nanocomposite gels projects, the Small Angle Neutron Scattering (SANS) experiment was carried out on NG3 and NG7 SANS instruments at the Center for Neutron Research, National Institute of Standards and Technology; the rheology of the nanocomposite gels was done on a TA ARES rheometer in our lab. The rheology and SANS are most important, and the facility for these experiments should be introduced in detail.

1.2.1 TA ARES rheometer

A rheometer is a sensitive measurement technique widely used to measure the rheology of materials, with a setup as shown in Fig.1- 4.

Fig. 1-4 A picture of the TA ARES rheometer.

For different samples, we may use different geometries to hold the samples. Generally, plate-plate is applied for solid material, cone-plate is applied for gels and non dilute solutions, while Couette is applied for dilute solutions. We mainly used our home made cone plate geometry in our experiments. The

cone and plate were stainless steel, with a cone diameter of 50 mm and cone angle of 2º. The plate diameter was 54 mm, 4 mm larger than the cone diameter to reduce edge effects. The plate had a lip at the perimeter to prevent material loss. The cone structure makes the shear rate the same at different locations. A bigger cone diameter and smaller cone angle can lead to a more precise measurement. As the measured data may also depend on the material of cone and plate, we used a standard sample to calibrate the machine for first time use.

There are two modes for the measurement, steady mode and dynamic modes. We must make the choice before we calibrate the distance between the cone and plate, and before we put any sample in it. In steady mode, we can use shear rate sweep to measure shear viscosity of a material. In dynamic mode, we may use frequency sweep to check how the elastic modulus, loss modulus, phase angle, and complex viscosity depend on the frequency. It is especially important to find the gel point because an important property at gel point is that the phase angle is almost independent of frequency. In this mode, we can also use temperature sweep to check the temperature dependence of the material, use strain sweep to check how the structure inside the material alters as the strain increase, and use time sweep to check how the material relaxes.

As the rheometer is a sensitive instrument, we must develop good habits in operating and maintaining this machine.

- First and foremost, we must check if the air pressure is high enough before we turn on the machine. As the motor is driven by the air pressure, the motor will be broken if the pressure is not high enough. We even need to put something over the motor while not in use, in case other people may touch this sensitive instrument.

- We must check if we have chosen the correct mode before we load any sample because we can't change mode when there is sample mounted.

- We should always move the sample holders in a gentle way in case they may collide and cause imprecision or even damage to the machine.

- We should always keep an eye on the normal force and torque indicated by the machine when we load sample and make measurement because they can never be out of the range accepted by the machine.

- It is always safer to take the sample holders out of the machine and then clean the sample than to clean the sample directly in the machine.

1.2.2 Small angle neutron scattering

Small angle neutron scattering (SANS) is a very powerful tool to study the microstructure of materials. A series of SANS experiments have been employed at the National Institute of Standard and Technology to study the shear induced structure of nanocomposite gels. Here I will introduce the basic theoretical background and application regarding SANS based on my friend, Min Y. Lin's lecture notes. [83]

Neutrons interact with matter through their nuclei. The scattering is very short range, and isotropic. As a result, the scattering from a single nucleus can be characterized by one parameter, b, called the scattering length. That is, b replaces the scattering amplitude, $f(\theta)$, in the scattering formula for neutrons scattered by one nucleus,

$$\psi(r) = \exp(i\vec{k}\bullet\vec{r}) - b\exp(i\vec{k}'\bullet\vec{r}) \tag{1.1}$$

where k is the wave vector of the incident wave, and k' is the wave vector of the scattered wave. In elastic or quasi-elastic scattering, $k' = k = 2\pi/\lambda$.

There is no complete theory of the nucleon – nucleon interaction. The scattering length b for each isotope has been tabulated by experimental measurements. It can be complex; the imaginary part represents absorption and usually is very small. Most importantly, b varies with Z, the atomic number, and can be different for different isotopes. To neutrons, matter is a collection of nuclei, each at a position r_i. The potential is therefore:

$$V(r) = \frac{2\pi h^2}{m}\sum_{i=1}^{N} b_i\delta(r - r_i) \tag{1.2}$$

Where all b_i are "coherent" scattering lengths of the isotopes, m is the mass of a nuclei, h is Planck's constant.

The scattering wave vector is $\vec{q} = \vec{k}' - \vec{k}$, and it's magnitude is

$$q = 2k\sin\theta = \frac{4\pi}{\lambda}\sin\theta \tag{1.3}$$

For SANS, the angle θ is small, typically $\theta < 15^o$. As small angles, $\sin\theta \cong \theta$; the range of q is only limited by the technical configuration of the small angle instrument. Another consequence of the length scales is that distances between nuclei (atoms) are small. Therefore, it is safe to average the scattering lengths into a density within a microscopic phase. It is called the neutron scattering length density

$$\rho = \frac{1}{v_m} \sum_{i=1}^{N} b_i n_i \tag{1.4}$$

One example is where one phase is particles, and the particles are made of one type of molecules. Then the average is over one molecule only, where N is the number of isotopes, n_i is the number of atoms of the ith isotope, b_i is the scattering length of that isotope, and v_m is the molecular volume.

For one particle in another phase ρ_0, e.g., solvent, the scattering cross section is:

$$d\sigma/d\Omega = |f(\theta)|^2 = (\rho_0 - \rho)^2 \left| \int \exp(-i\vec{q} \bullet \vec{r}) dr \right|^2 \tag{1.5}$$

Now the integral is over the particle volume v only. The cross section depends on the size, shape and orientation of the particle only, independent of the particle position. The factor $(\rho_0 - \rho)^2$ is called contrast. In neutron scattering it can be varied relatively easily by isotope substitution without changing the material's property.

In experiments, small-angle neutron or X-ray scattering (SANS and SAXS) reveal the structure of amorphous materials in the range of length scales between 1 and 100 nm. This resolution is of particular interest in the field of polymers solutions and gels. In the simplest case of a dilute polymer solution, two length scales are required to describe the system: that of the local chemical architecture, i.e., the length of the repeating unit, and the radius of gyration, R_G, of the individual coils.[84] In more concentrated solutions, as the coils overlap they lose their individuality, and the thermodynamic properties are governed by another length scale, ξ, the

correlation length between polymer segments.[85] In this overlapping (semidilute) regime, however, an additional length scale arises-the distance between entanglements along a given chain, which controls primarily the dynamic response through the plateau modulus of the solution.[86] In a chemically cross-linked network, the situation is more complex: (i) the presence of cross-links imposes permanent constraints on the network chains; (ii) rearrangements of the polymer segments occur that depend on the details of the cross-linking procedure. These superstructures are detectable at high degrees of swelling, where they appear as concentrated regions embedded in a more dilute background. Neutron scattering is a powerful tool for revealing the spatial extent of these longer range supermolecular structures, which control the overall physical behavior of the network both in the dry and in the swollen state.[87, 88]

When the length scale is bigger than 100 nm, we need q to be even smaller, meaning the angle θ should be small. In this case, SANS may not be able to satisfy our requirement, instead USANS (Ultra Small Angle Neutron Scattering) will work in this regime. In the NG7 BT5 USANS instrument at Center for Neutron Research of the National Institute of Standards and Technology, the q range can run from 3.33E-4 nm^{-1} to 1.05E-2 nm^{-1}, indicating the scattering scale range can be from 100nm to 3000nm.

1.3 Thesis Structure

In this thesis, we will introduce our research work on two projects: spin cast nanocomposite films and nanocomposite gels. Chapter 2 and Chapter 3 are for nanocomposite films projects; Chapter 4 and Chapter 5 are for

nanocomposite gels. Actually each chapter comes from an independent paper for a journal publication; they may overlap in some parts.

Chapter 2 is based on a paper published as Applied Physics Letters 89, 111917 (2006). In this Chapter we mainly discuss the orientation effect of clay in spin cast nanocomposite films. We show that the thickness of spin cast nanocomposite polystyrene/clay films displays a large radial dependence that is not explained by current models. Transmission electron microscopy and atomic force microscopy reveal a tendency for the high aspect ratio clay particles to align in the direction of shear. Near the center of rotation, particles remain randomly oriented, leading to the formation of voids as the film dries. We present a two dimensional numerical model that incorporates both hydrodynamic and orientation effects, and accurately fits the thickness data over a wide range of filler concentrations and spin rates.

Chapter 3 will further introduce the experiments and model development, and it will be a paper to be submitted to the Journal of Applied Physics. This Chapter is actually a full paper following a letter. In this chapter, we show additional evidence that spin-cast polystyrene (PS)/Cloisite 6A (clay) nanocomposite films display a large radial thickness dependence that increases with clay concentration. A numerical model has been developed to calculate the film thickness distribution based on mass transfer. The model requires knowledge of shear dependent viscosities and evaporation rates as a function of clay and solvent (toluene) concentration. We report detailed measurements of these parameters, and show that they are well described by standard models. Shear thinning cannot account for the strong radial dependence, but extending the model to include the effect of clay platelet orientation provides a good fit to experimental data. Transmission Electronic

Microscopy (TEM) cross-sections show that the clay platelets are randomly oriented near the axis of rotation, but become increasingly aligned at greater distances from the axis.

Chapter 4 is based on a paper that has been published as Macromolecular Rapid Communications 27, 1787 (2006). In this chapter, we mainly discuss the temperature effect on shear induced anisotropic structure in polymer clay hydrogels. Shear induced orientation of nanoparticles in Poly(ethylene oxide)/ Laponite RD hydrogels has been investigated by small angle neutron scattering (SANS). As temperature is reduced, anisotropy develops at lower shear rates. The two correlation length Debye-Anderson-Brumberger (DAB) model provides a good fit to the experimental data. The deduced short range correlation length (~5 nm) is observed to increase with shear. The long range correlation length (~ 50 nm) shows a strong directional dependence, and decreases when shear is applied. The relative contribution of long range order to the SANS intensity is observed to increase with shear and decrease with temperature.

Chapter 5 will discuss the concentration effect on shear induced structure and dynamic response in nanocomposite hydrogels, which is complementary to Chapter 4. It is a paper that will be submitted to Europhysics Letters for publication. Shear induced structures of PEO/ LRD hydrogels with different concentration have been investigated by SANS. The anisotropic SANS patterns develop at a lower shear rate when the weight concentration ratio between PEO and LRD is about 1:2. The two correlation length DAB model provides a good fit to the experimental data. The deduced short range correlation length will increase with the polymer clay volume ratio when it is bigger than a threshold value. The long range correlation length

shows a strong directional dependence, and decreases when shear is applied, but the relative weight of long range correlation will increase with shear rate. The rheology data show that the system becomes very elastic, and the network inside is optimal at a specific weight concentration ratio.

Chapter 6 will provide a summary for the whole thesis, and it will point out what work has been left for further study.

Chapter 2

EFFECT OF CLAY PLATELET ORIENTATION ON SPIN CAST NANOCOMPOSITE FILMS[1]

2.1 Introduction

Spin cast films are widely employed in device manufacture, and in fundamental studies of novel thin films.[90] During the spin-casting process, competition between solvent evaporation and viscous spreading typically results in a film of uniform thickness. The addition of clay nanoparticles allows the creation of nanocomposite films with enhanced control over such properties as gas permeability and flame retardance.[1,91] In solution, the clay may exfoliate into a large number of platelets, each only a few nanometers in thickness. The platelets orient under shear, producing a non-Newtonian solution that is well described by the Carreau model. Jenekhe and Schuldt[92] predict that a Carreau model fluid should still produce a spin cast film of uniform thickness. Britten and Thomas[93] have examined spin cast films from non-Newtonian colloidal suspensions of spherical silica particles, and of plate shaped alumina particles, in methanol. In the former case, uniformly thick films were indeed produced, while for the elongated particles, the film thickness dropped by only a few percent from the center to the periphery of the film. We have spun cast solutions of high molecular weight polystyrene with different concentrations of functionalized clay, and mapped the radial thickness variation. We show that the film thickness varies by as much as a

[1] This chapter has been published at Applied Physics Letters 89, 111917 (2006) [89]

factor of four over a radial distance of several millimeters, as illustrated in Fig. 5. We describe a quantitative model which correlates the orientation of the clay platelets with the film thickness and predicts the observed thickness variations as a function of spinning parameters.

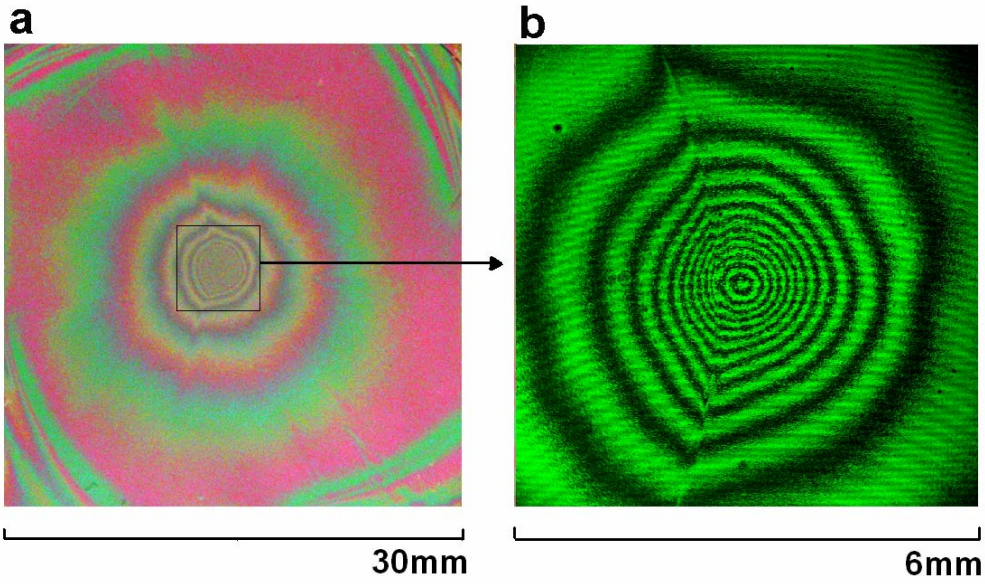

Fig. 2-1. A nanocomposite flm spun cast on silicon at 3000 rpm for 30 s from a solution of PS (60mg/ml)/Cloisite 6A (30mg/ml)/toluene. The film thickness is ~ 4 μm in the center, decreasing to ~ 4 μm at the periphery. a) Photograph (Nikon Coolpix 4500) of the film. b) confocal microscope image (Leica TCS SP2) of the central region as indicated.

2.2. Experiment

Spin cast film thicknesses were examined for mixtures of polystyrene (Mw 280K, Aldrich), Cloisite 6A (Southern Clay), and toluene (99.5, Aldrich). The PS concentration was held fixed at 60 mg per ml toluene, with clay concentrations of 0, 10, 20, 30, and 40 mg/ml. The solutions were treated with

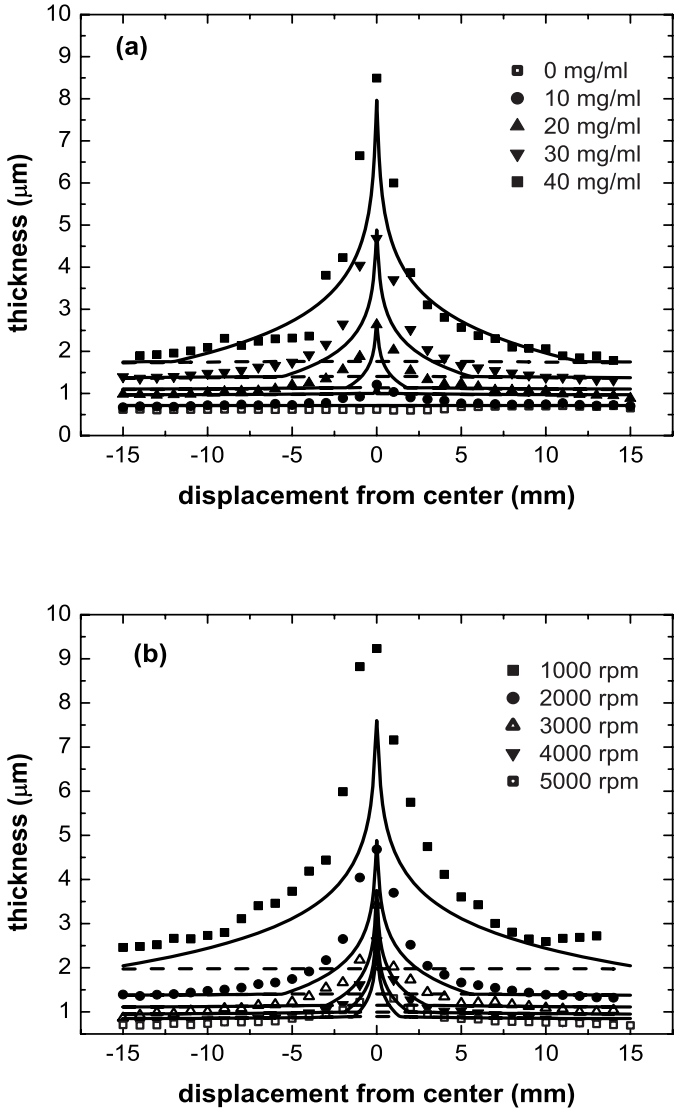

Fig. 2-2. PS/clay/toluene spin cast films. The symbols represent measured data. The dash lines are the prediction of the mass transfer model. The solid lines are predicted by the orientation model. (a) spin rate 2000 rpm, PS 60 mg/ml, clay concentrations as indicated. (b) PS 60 mg/ml, clay 30 mg/ml, spin rates as indicated.

ultrasound for periods of at least one hour to assist clay exfoliation. A Headway spinner was used to spin cast the nanocomposite film onto as-received silicon. The dry nanocomposite films displayed concentric rings (Fig. 1-1), with the center of the rings clearly identifying the rotation axis. A Dektak IIA surface profilometer was employed to measure thickness at different wafer locations. A line was scribed with a razor blade through the center of rotation, and the thickness measured at 1 mm intervals. For a spin rate of 2000 rpm (30 s duration), the film thickness increases as the clay concentration increases, and shows a strong radial dependence when the clay concentration is high (Fig. 2-2(a)). The effect of spin rate was studied at a clay concentration of 30 mg/ml. From Fig. 2-2(b), it can be observed that thickness decreases as spin rate increases, and falls more rapidly to its perimeter value at the higher spin rates. The illustrated fits to the data are discussed below.

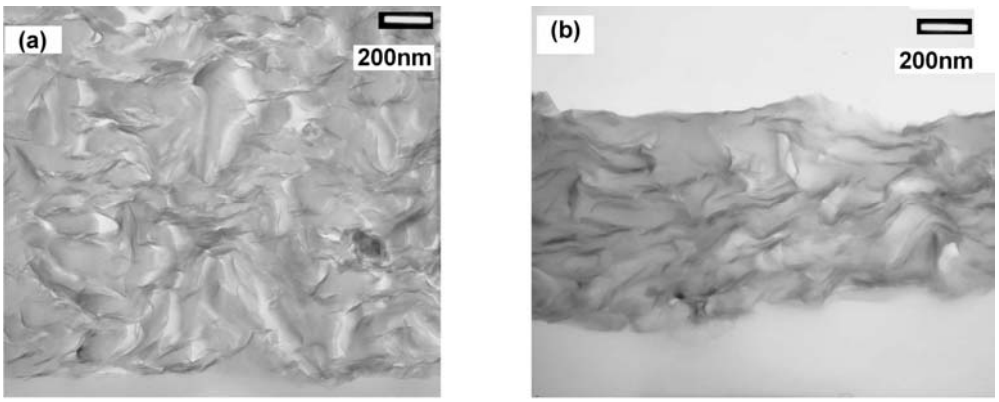

Fig. 2-3. Cross section TEM images of PS (60 mg/ml)/clay (40 mg/ml) spun cast films on vinyl cyclohexene substrate (a) center region, and (b) outer region.

Clay platelet orientation was examined by both transmission electron microscopy (TEM) and atomic force microscopy (AFM). A clay concentration of 40 mg/ml was employed for TEM analysis. Films were spin cast on vinyl cyclohexene substrates with a spin rate of 3000 rpm for 30 s. Samples were cut from the center and outer regions of the film, and a JEOL JEM1200 TEM was used to obtain cross section images. Fig. 2-3(a), from the center region, shows random clay platelet orientation and the presence of voids. Fig. 2-3(b), from the outer region, shows a tendency for the clay platelets to orient parallel to the surface of the substrate, due to the high shear rate.

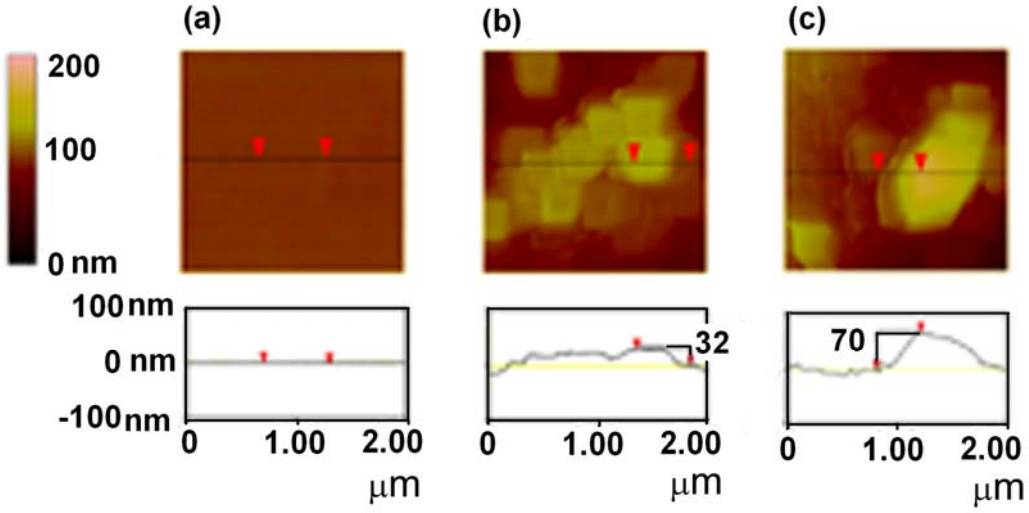

Fig 2-4. AFM topographical images of polymer films spun cast at 2000 rpm. (a) PS film without clay, (b) the outer region of a PS (60 mg/ml)/clay (10 mg/ml) film, and (c) the center region of the same PS/clay film.

AFM experiments were performed on samples with a PS (MW 50K, Pressure Chemical) concentration of 60 mg/ml, either with no clay or with a clay concentration of 10 mg/ml, spin cast at 2000 rpm for 30 s. An AFM Dimension 3000 was employed to scan a 2 μm × 2 μm at the center and outer regions of the films. The image of the center region of the sample with no clay (Fig. 2-4(a)) displays a smooth surface with a low density of surface asperities. Surface roughness develops in the sample with clay. In the outer region (Fig. 2-4(b)), individual platelets are clearly visible and well aligned with the film surface. In the central region (Fig.2- 4(c)), more steeply sloped surface asperities are observed. The rms height variations for the scan lines shown in Fig's 4(a), 4(b), and 4(c) are 0.53 nm, 12.6 nm, and 25.7 nm respectively. AFM was also employed to image individual platelets adhered to a silicon surface, prepared by a Langmuir-Blodgett technique. The average extent of the platelets was measured to be ~450 nm, consistent with the TEM results, as well as with Fig. 2-4(b). X-ray diffraction results of Lim and Park[94] show that the platelet thickness is about 3.5 nm.

2.3 Model

The dashed and solid lines in Fig. 2-2 are the result of model calculations. A mass transfer model[95] describes the time dependent film thickness during spinning as:

$$\frac{\partial h}{\partial t} = -\frac{\rho\omega^2}{3r\eta}\frac{\partial(r^2h^3)}{\partial r} - \tilde{e} \tag{2.1}$$

Where h is film thickness and is a function of radius r, t is time, ρ is the density of the solution, ω is spin rate, η is viscosity, and $\tilde{e}$ is evaporation rate. In this model, the mean square shear rate is given by

$$<\dot{\gamma}^2>=\frac{\int_0^h \dot{\gamma}^2 dz}{h}=(\frac{\rho\omega^2 h}{\eta})^2(\frac{6h^2}{5}+\frac{r^2}{3}) \qquad (2.2)$$

In order to apply Eq.(2.1), we must first determine the concentration dependence of viscosity and evaporation rate, as well as the shear rate dependence of the viscosity. The values of viscosity and evaporation rate both change by orders of magnitude during the spinning process. A TA ARES rheometer was employed to measure the static shear dependent viscosity of PS/clay/toluene solutions at room temperature in the cone plate geometry. The cone and plate were stainless steel, with a cone diameter of 50 mm and cone angle of 2^o. The shear dependent viscosities were found to be well described by the Carreau Equation[96]:

$$\eta-\eta_\infty=(\eta_0-\eta_\infty)(1+\lambda^2\dot{\gamma}^2)^{-N} \qquad (2.3)$$

η_∞ is the viscosity when shear rate is infinite, η_0 is the zero shear viscosity, λ is the relaxation time (the inverse of the shear thinning rate), and N is the negative of the slope of the shear thinning curve. These parameters depend on the polymer and clay concentrations. Evaporation rates in still air were determined by weight loss measurements for various polymer/clay concentrations. At high spin rates, the evaporation rate is known to increase in proportion to the square root of the spin rate[97,98]. By monitoring the weight loss of toluene in a spinning Petri dish, the transition to a square root dependence was observed to occur at ~100 rpm. The evaporation rate data

were well fit by assuming that the evaporation rate is proportional to the surface area of remnant toluene.

The mass transfer model was implemented by dividing the spin coating process into three stages: a brief initial spinning stage where evaporation is negligible, an intermediate stage that terminates when spinning is halted, and a final drying phase. In the short ~1 s initial stage, during which the film thickness may decrease by orders of magnitude as solution washes off the surface, it is reasonable to assume that the density, viscosity, and evaporation rate remain constant.[99] Eq.(2.1) then has a simple analytic solution. In the second stage, the incremental change of thickness in Eq.(2.1) due to evaporation and flow is calculated at time intervals of 1 ms, and radial intervals of 50 μm. After each time step, the local concentration and shear rate are recalculated, allowing updated values of viscosity and evaporation rate to be used for the next iteration. In the final drying stage, the calculation continues at zero spin rate until the film reaches its final thickness. The model is two-dimensional, and of necessity ignores possible variations of platelet density with depth, but the TEM images suggest a relatively uniform distribution. The results of the model calculations (Fig. 2-2) adequately describe the effect of concentration and spin rate in the outer region of the samples, but predict a very small dependence on radius. Britten and Thomas[93] employed a similar model, also predicting a weak dependence on radius despite the highly non-Newtonian nature of their colloidal system.

In order to model the effect of platelet orientation, we develop an estimate for the orientation order parameter

$$S = < (3COS^2\delta - 1)/2 > \qquad (2.4)$$

at all locations on the sample, where δ is the deviation angle of the particle with respect to the flow direction. When all particles are aligned in the direction of flow, the parameter *S* is equal to 1, while for purely random orientation, *S* is equal to 0. Förster et al.[100] have shown that, for an experimental system of cylindrical micelles, the viscosity is given by:

$$\eta = \eta_0 e^{-aS} \tag{2.5}$$

The parameter, *a*, has a value of ~13.8 over a wide range of micelle concentrations. Inserting into Eq.(2.3) with the approximation $\frac{\eta_\infty}{\eta_0} \approx 0$, we obtain:

$$S = \frac{N}{a}\ln(1+\lambda^2\dot{\gamma}^2) = \frac{N}{a}\ln(1+\frac{\dot{\gamma}_m^{\ 2}}{\dot{\gamma}_c^{\ 2}}) \tag{2.6}$$

Here, $\dot{\gamma}_m^{\ 2}$ is the maximum mean square shear rate encountered in the numerical simulation at a given location, and λ is derived from the fit of Eq.(2.3) to viscosity data. We obtain an estimate of film thickness by assuming, first, that the mass transfer model correctly describes the film thickness up to the point in time where shear flow becomes negligible, and second, that during subsequent evaporation, the clay/polymer domains cannot reorient. As polymer chains attach to both platelet surfaces and move with it, comprising a clay/polymer domain, the thickness of a domain, h_o, is on the order of the radius of gyration, ~20nm. Randomly oriented domains extend over a vertical distance, h_r, on the order of $(450\times 450\times h_o)^{\frac{1}{3}}$ or 160 nm. For

partial orientation, we employ a simple empirical formula to estimate the average vertical extent h_S of a domain in the film:

$$h_S = h_o \times S + h_r \times (1 - S) \tag{2.7}$$

The number of domains stacked vertically, *n*, is easily found from the final calculated clay volume, so the net contribution to the film thickness is nh_S . If the film thickness in the numerical simulation is observed to drop below nh_S , the thickness at the conclusion of the simulation is reported as nh_S . The clay/polymer domain orientations are fixed at this stage, so that additional solvent evaporation results in the presence of voids within the film. The solid lines in Fig. 2-2 show the prediction of the model with the effect of platelet orientation included, and provide a much better fit to experiment.

2.4 Conclusion

We have shown in the PS/Cloisite/toluene system that the orientation of high aspect ratio filler particles has a strong effect on spin cast film thickness, surface roughness, and void formation. The radial dependence of the film thickness as a function of the spinning parameters can be modeled accurately by accounting for orientation effects, and the shear rate required to suppress void formation can be predicted.

Chapter 3

STRUCTURE AND THICKNESS MODELING FOR SPUN CAST POLYSTYRENE/CLAY NANOCOMPOSITE FILM

3.1 Introduction

Spin coating is widely employed to create thin films because it is inexpensive and can be applied to large areas. This technology is used in the manufacture of integrated circuits, magnetic storage disks, and optical devices, and in recent years has been applied to fabricate field effect transistors[89,101], solar cells,[102,103] and light-emitting diodes[104,105] as well. Hybrid films, such as polymer/silica composites, have the potential to improve device performance.[106] Such films can be prepared by spin-casting a solution of polymer and composite onto a substrate such as silicon wafer or glass surface. In the spin-casting process, film thickness depends on a competition between viscous spreading of the film and solvent evaporation during the spinning process. Emsli, Bonner and Peck[107] first described the flow of a viscous liquid on a rotating disk. Since then, a number of theoretical models have been developed to calculate the thickness of spin cast films.[92,93,95,108-115] These models are not easily applied to nanocomposite systems. Introduction of particles into the polymer solution produces a shear-dependent viscosity, and anisotropic composite particles may orient during the process of spinning and thus modify the film structure. In this paper we examine the structure of spin-cast films of polystyrene (PS)/clay

(Cloisite 6A) dissolved in toluene. We observe that the orientation of exfoliated clay platelets has a profound effect on film thickness.

The introduction of clay into the polymer matrix can improve mechanical properties[1,116] and gas permeability.[117,118] When clay is introduced into a polymer solution, it can exfoliate into a large number of platelets. All polymer chains in the resulting spin-cast film are then close enough to a clay surface to be affected by local interactions. Under shear, polymer/platelet domains orient to produce a shear thinning effect. During spinning, shear rate increases with radius, so viscosity varies with radius. We show that a model for spin-cast film thickness must account for the effects of platelet orientation.

During spinning, the centrifugal force is balanced by the viscoelastic force when the solution is in dynamic equilibrium. The flow along the tangential direction becomes negligible at short spin times, so that mass transfer is mainly due to radial flow and evaporation of solvent. As in prior models, we employ this approximation. We measure the shear dependent viscosity and evaporation rate as a function of clay and solvent concentration, and find that these data are well fit by standard models. Thus we are able to use a numerical simulation to predict the radial dependence of film thickness. Comparing the calculated result with experimental data, we find that the film thickness near the axis of rotation is grossly underestimated, indicating that the radial dependence can not be fully explained by the mass transfer model. We believe that the orientation of PS/clay domains is the main reason for the observed discrepancy. This hypothesis is supported by TEM cross-sections of spin-cast PS/clay nanocomposite films. We therefore incorporate a simple orientation model

into the mass transfer model. The calculated results of this new model provide a good fit to the experimental data.

3.2 Experiment

3.2.1 Thickness of spin cast PS/clay/toluene films

Polystyrene (Mw 280K, Aldrich), Cloisite 6A (Southern Clay) and toluene (99.5%, Aldrich) were mixed together. The PS concentration was initially held fixed at 60mg/ml, while the clay concentration varied as 0mg/ml, 10mg/ml, 20mg/ml, 30mg/ml and 40mg/ml. (In the latter sample, for example, the solution would consist of 60 mg PS, 40 mg clay, and 1 ml toluene.) The solutions were treated with ultrasound for periods of at least one hour to help the clay exfoliate. A Headway spinner was used to spin cast the nanocomposite film onto fresh hydrophobic silicon wafers with size about 30mm × 30mm.

When the films were dry, for those films with clay, we could clearly see a rainbow colored set of concentric rings on the surface. The center of the rings locates the spinning axis. As the films with clay were strongly scattering, the ellipsometer could not measure the thickness correctly. Instead, a Dektak IIA surface profilometer was applied to measure film thickness at different locations on the wafer. A line was scribed with a razor blade through the center of rotation. Thickness was measured at 1 mm

intervals. In pure PS films, the surface profilometer and ellipsometer measurements were in good agreement.

For a spin rate of 2000 rpm and a spin time of 60 s, the measured film thicknesses are shown in Fig. 3-1 as discrete symbols. The film thickness increases as the clay concentration increases, and shows a strong radial dependence when the clay concentration is high.

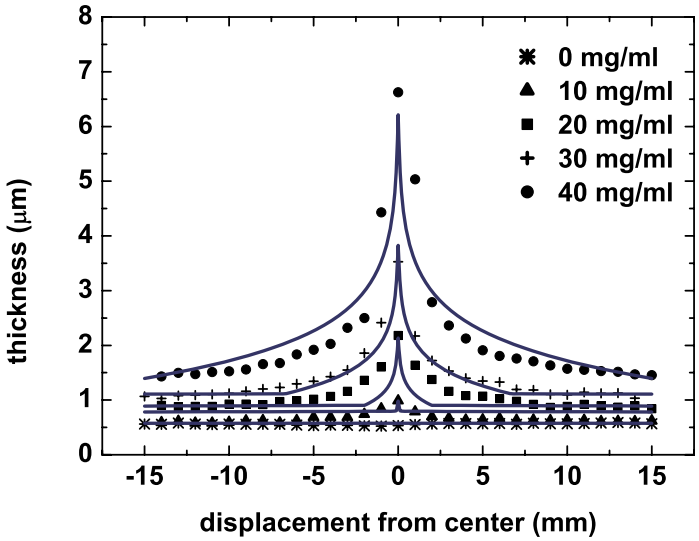

Fig. 3-1. The effect of clay concentration on the thickness distribution for PS/clay/toluene spin cast films, PS concentration is 60mg/ml and clay concentrations vary as indicated. The spin rate was 2000 rpm, spin time was 60 s, and the treated silicon wafers were hydrophobic.

To examine the effect of spin rate, we set the clay concentration at 40 mg/ml, set the spin time at 30 s, and spin rate at 1000 rpm, 2000 rpm, 3000 rpm, and 4000rpm. From Fig. 3-2, it can be observed that film thickness

decreases as spin rate increases. The radial dependence for film thickness is still strong in all cases, and the slope of the films is enhanced at higher spin rates.

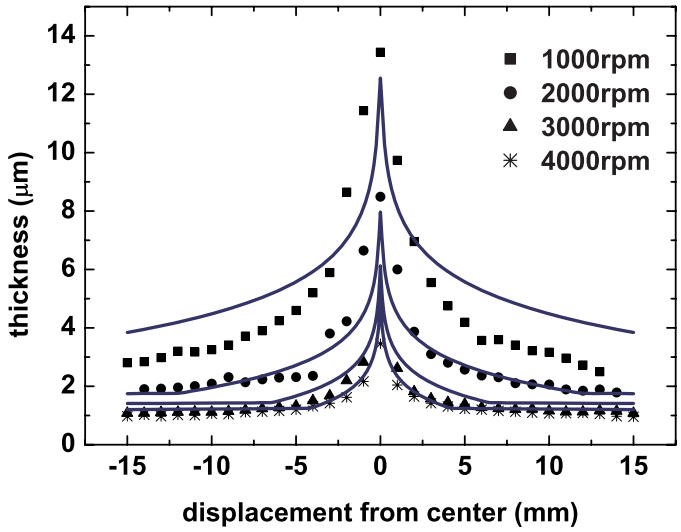

Fig. 3-2. The effect of spin rate on the thickness distribution for PS/clay/toluene spun cast films on as received silicon wafers for a PS concentration of 60 mg/ml and clay concentration of 40mg/ml . The spin time is 30 s, spin rates vary as indicated.

3.2.2 TEM cross sections

A clay concentration of 40 mg/ml was employed for TEM analysis. Several films were spin cast on vinyl cyclohexene substrates with spin rate at 3000 rpm and spin time at 30 s. Two samples were cut from the center of the films along the radial direction and tangential directions, respectively. Another two

samples were cut from the periphery of the films, again along the radial and tangential directions. A JEOL JEM1200 TEM was used to obtain images of these samples, as shown in Fig. 3-3. Images 3a and 3b from the central region show random clay platelet orientation. On the other hand, images 3c

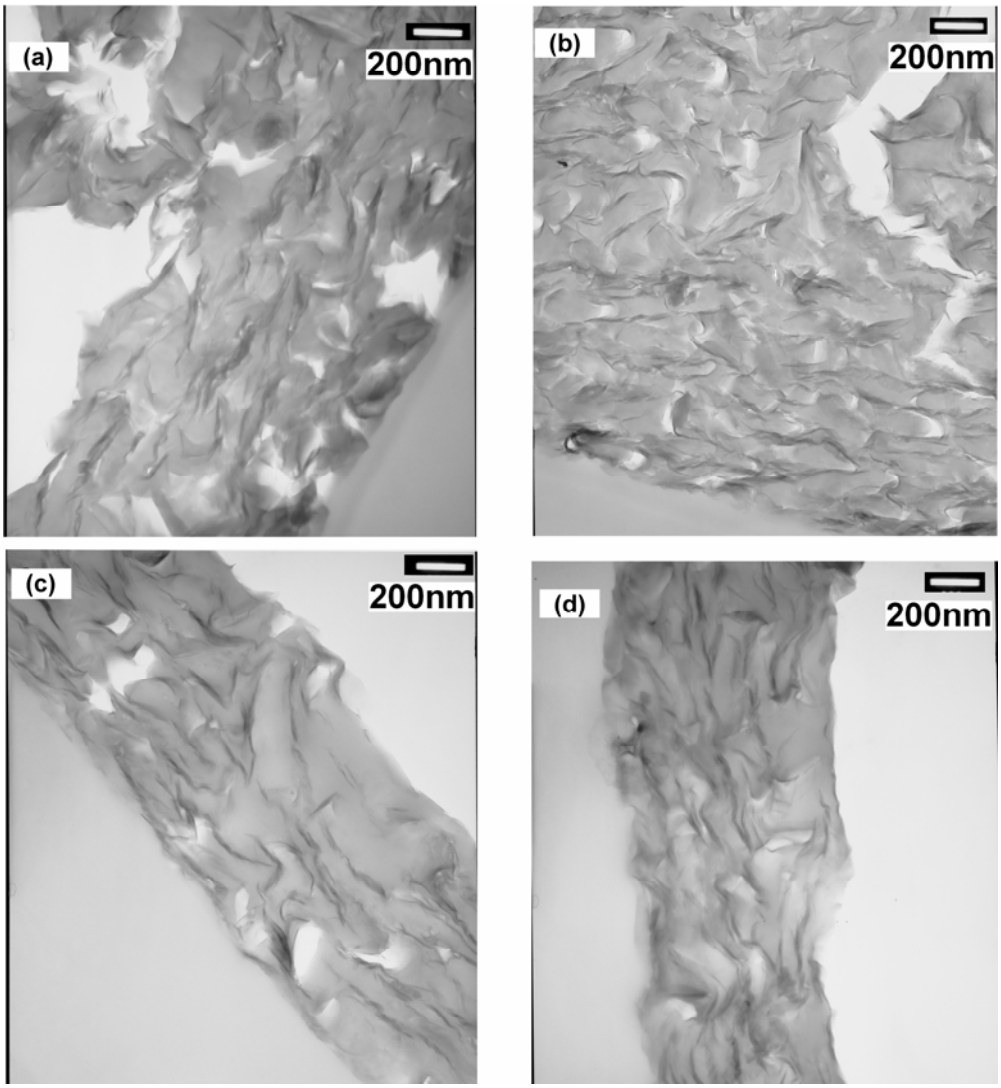

FIG. 3-3. Cross Section TEM pictures for PS/clay spin cast films on vinyl cyclohexene substrates with a PS concentration of 60 mg/ml, clay

concentration of 40 mg/ml, spin rate of 3000 rpm, and spin time of 30 s. (a) Cross-section cut from the center region along a radial direction. (b) Cross-section cut from the center region along a tangential direction. (c) Cross-section cut from the outer region along a radial direction. (d) Cross-section cut from the outer region along a tangential direction.

and 3d from the outer region of the films show a tendency for the clay platelets to orient parallel to the surface of the substrate, presumably due to the high shear rate.

3.2.3 Atomic Force Micrographs (AFM) of a Langmuir-Blodgett Cloisite 6A film

A solution of Cloisite 6A (Southern Clay) in toluene (99.5%, Aldrich) was prepared with concentration 1mg/ml, and then treated by ultrasound for one hour to induce exfoliation. An as-received silicon wafer with size about 3 cm × 3 cm was chemically treated so as to be hydrophilic. The silicon wafer was fastened to the dipper of a KSV 5000 LB trough and then the dipper descended so that 90% of the silicon wafer was immersed in deionized water. 50 μl of the aforementioned Cloisite toluene solution was then dispersed at the air-water interface. After toluene had evaporated and surface tension was smaller than 0.2mN/m, the barrier was translated at a speed of 5 mm/minute to compress the surface film. When the surface tension reached 7.8 mN/m, the barrier motion ceased. The silicon wafer then moved upward at a speed of 2 mm/minute. The resulting Cloisite 6A Langmuir-Blodgett film was then scanned with an AFM Dimension 3000. Despite significant aggregation of

particles, some platelets are visible in the AFM micrograph of Fig. 3-4. The average extent of those platelets is about 450 nm, consistent with the TEM micrographs (Fig. 3-3). Lim's x-ray diffraction experiments[94] showed that the platelet thickness is about 3.5 nm.

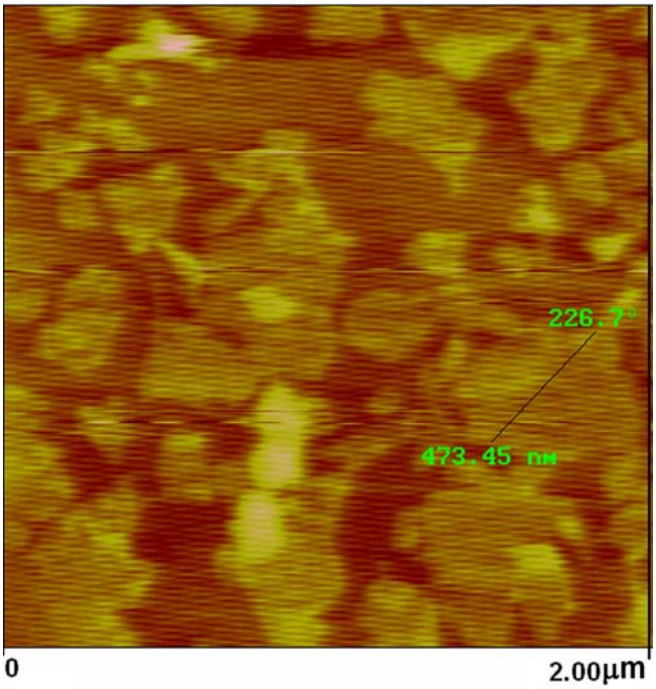

FIG. 3-4. AFM micrograph of a Cloisite 6A Langmuir-Blodgett(LB) film deposited on a silicon substrate. The line indicates a platelet dimension of 473 nm.

3.2.4 Viscosity

Viscosity is a function of the polymer concentration C_p, clay concentration C_c, shear rate, molecular weight and temperature. In the present experiments,

molecular weight and temperature were held constant. Our nanocomposite solutions are non-Newtonian, and the well accepted Carreau Model[96] is chosen to describe the viscosity dependence on shear rate:

$$\eta - \eta_\infty = (\eta_0 - \eta_\infty)(1 + \lambda^2 \dot{\gamma}^2)^{-N} \tag{3.1}$$

η_∞ is the viscosity when shear rate is infinite, η_0 is the zero shear viscosity, λ is the relaxation time (the inverse of the shear thinning rate), and N is the negative of the slope of the shear thinning curve. All four parameters depend on C_p and C_c.

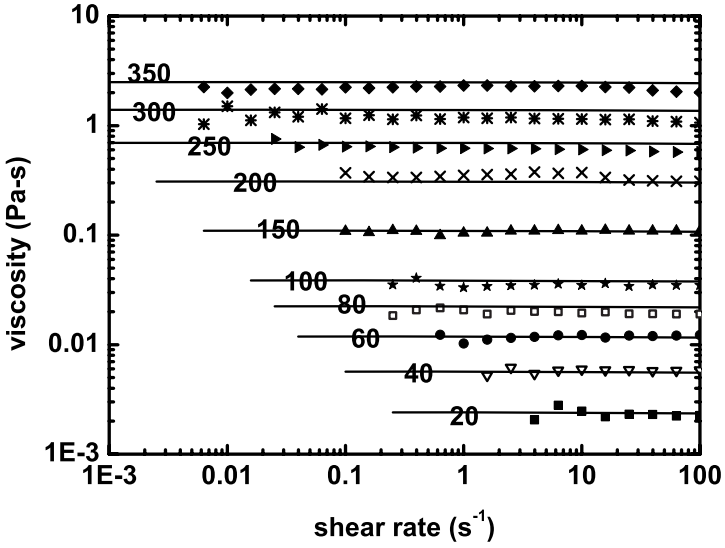

Fig. 3-5. Viscosity of PS/toluene solutions as a function of shear rate, were measured by a TA ARES rheometer in the cone plate geometry. The numbers represent the PS concentration of each sample in units of mg/ml. The solid lines indicate the magnitudes predicted by Eq. (2).

A TA ARES rheometer was applied to measure the static viscosity of PS/toluene solutions at room temperature in the cone plate geometry. The cone and plate were stainless steel, with a cone diameter of 50 mm and cone angle of 2º. The plate diameter was 54 mm, 4 mm larger than the cone diameter to reduce edge effects. The plate had a lip at the perimeter to prevent material loss. Successive measurements confirmed that evaporation during the measurement had a negligible effect. A commercial viscosity standard was employed for calibration.

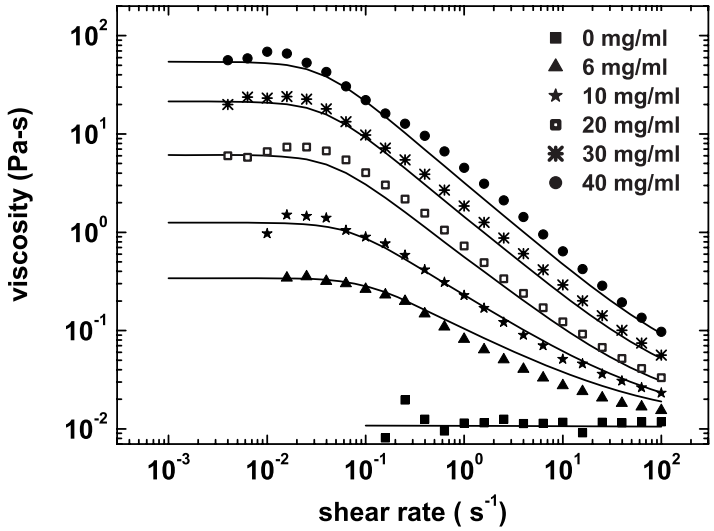

Fig. 3-6. Viscosity of PS/clay/toluene solutions as a function of shear rate. The PS concentration is 60 mg/ml, while the clay concentration varies as indicated. The solid lines are plots of Eq. (3.1).

The experimental data are shown in Fig 3-5. Negligible shear thinning is observed at low PS concentration. As shown in the figure, the viscosity is well fit by the function:

$$\ln(\eta_{ps}) = 3.322 - 6.067e^{-C_P / 226.6} \qquad (3.2)$$

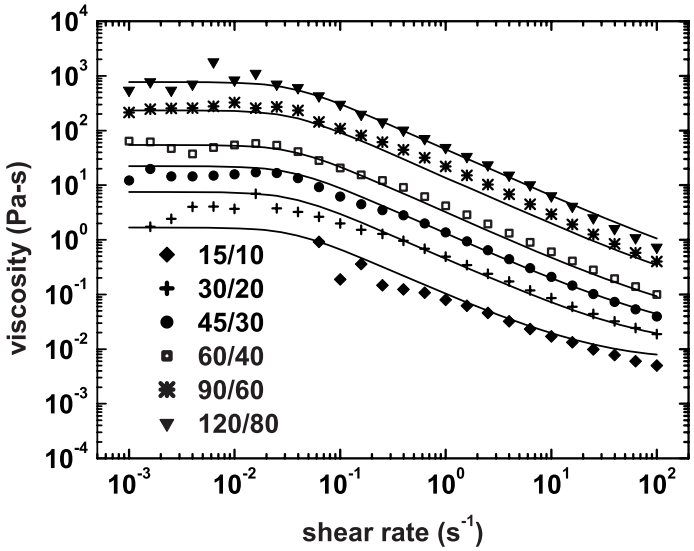

Fig. 3-7. Viscosity of PS/clay/toluene solution for PS/clay concentration ratios of 3/2. The numbers represent the PS concentration/ clay concentration of the sample in units of mg/ml. The solid lines are plots of Eq. (3.1).

PS/clay solutions were ultrasonicated for several hours. After all the clay and PS had dissolved and the solution appeared homogeneous, the viscosity was examined as before. Fig. 3-6 shows data for fixed PS concentration (60

mg/ml), while Figure 3-7 displays data for a fixed ratio Cp/Cc of 3/2. The solid lines in both figures indicate that the data is well fit by the Carreau model, Eq. (3.1). The four parameters in the equation are observed to vary smoothly with concentration, and are described by simple empirical functions in the simulations below.

3.2.5 Evaporation rate

Evaporation rate is a function of spin rate[97,98], and the concentrations of polymer and clay. During spinning, the evaporation rate $\{\tilde{e}\}$, with units of m/s, is popularly described by:

$$\tilde{e} = K_e \sqrt{\omega} \tag{3.3}$$

K_e is a scaling constant determined by experiment. It implicitly includes such effects as the solvent's vapor pressure over the solution, diffusion rate in air, and parameters that control the vapor boundary layer thickness. For the purpose of numerical simulations, we will require a formula for the evaporation rate as a function of polymer and clay concentrations. While an empirical formula could prove adequate, we show here that a simplistic physical model provides a good description of measured evaporation rates.

We assume that the evaporation rate is proportional to the surface area of free solvent, and when the evaporation ceases, the concentration of the polymer is C_f (in mg/ml) and the volume of trapped solvent is V_f. If we let V represent the total solvent volume in the solution, then:

$$\tilde{e}_0 \propto \left(\frac{V - V_f}{V + V_{polymer} + \alpha \times V_{composite}}\right)^{2/3} = \left(\frac{\frac{1}{C_p} - \frac{1}{C_f}}{\frac{1}{C_p} + \frac{1}{\rho_p} + \frac{\alpha}{\rho_c}\frac{C_c}{C_p}}\right)^{2/3} \tag{3.4}$$

Here, α is a dimensionless parameter that accounts for the high aspect ratio of the clay platelets. If the platelets were cubic in shape, α would have a value of 1, but because they tend to be aligned with the solution surface, evaporation is greatly reduced. A value of α = 50 is employed to fit the observed data below.

According to Eq. (3.3), we know that the square of the evaporation rate is proportional to the spin rate. A series of experiments were first carried out to test this relationship for pure toluene. During the measurement, toluene was placed in a glass dish with a diameter of 5.76 cm and height of 1.0 cm. We first measured the evaporation rate when the dish was stationary in an open fume hood with face velocity 100 ft/m. We then employed a mass balance to measure the evaporation rate at different spin rates in five minute cycles. During each cycle, the dish was spun for 100 s at a selected spin rate, and spent another 200 s without spinning prior to measurement of the mass of the dish. As the stationary evaporation rate had already been determined, it was thus possible to determine

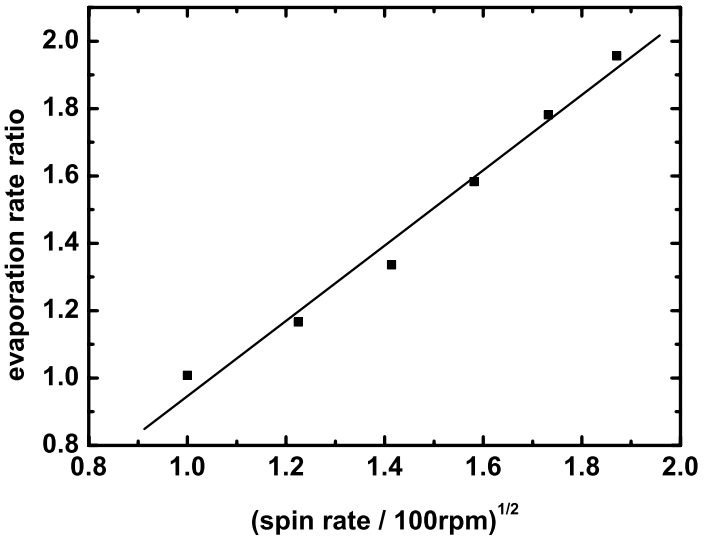

Fig. 3-8. The normalized evaporation rate, y, determined by mass loss measurement, is plotted as a function of (spin rate/100 rpm)$^{1/2}$, x. The linear fit is given by $y = 1.12\,x - 0.17$.

the evaporation rate during spinning. In these experiments, the evaporation did not change significantly until the spin rate increased above 100 rpm. When the spin rate is smaller than 100 rpm, the evaporation rate is assumed to be $\tilde{e}_0$. Fig. 3-8 shows that Eq. (3.3) provides a good description of the toluene evaporation rate at spin rates above 100 rpm.

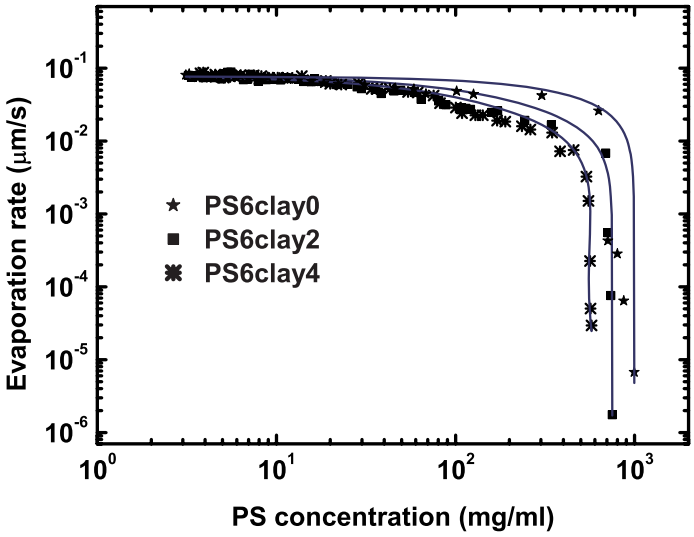

Fig. 3-9. Evaporation rate ratio vs PS concentration, as determined by mass loss measurements, PS/clay concentration ratios vary as indicated.

The concentration dependence of Eq. (3.4) was also examined experimentally. PS (Mw 280K, Aldrich), Cloisite 6A, toluene dilute solutions were used with clay/ PS concentration ratios set at 0/3, 1/3 and 2/3. As before, the solutions were treated with ultrasound to induce exfoliation. Evaporation rates were determined by mass loss measurements as just described, and the experimental results are shown in Fig. 3-9. The data are well described by Eq. (3.4).

3.3 Model

3.3.1 Mass transfer model

We divide the spin coating process into three stages: a brief initial spinning stage where evaporation is negligible, an intermediate stage that terminates when spinning is halted, and a final drying phase where evaporation may continue to significantly reduce the film thickness. The time dependent film thickness during spinning has been described as:

$$\frac{\partial h}{\partial t} = -\frac{\rho\omega^2}{3r\eta}\frac{\partial(r^2h^3)}{\partial r} - \tilde{e} \tag{3.5}$$

where h is film thickness and is a function or radius r, t is time, ρ is the density of the solution, ω is spin rate, η is viscosity, and $\tilde{e}$ is evaporation rate. During the short (~1 s) initial phase, it is reasonable to assume that the density, viscosity, and evaporation rate remain constant, and that the evaporation rate term is small. In this case, a film of uniform thickness remains flat as a function of time. Eq. (3.5) simplifies to:

$$\frac{\partial h}{\partial t} = -\frac{2\rho\omega^2h^3}{3\eta} - \tilde{e} \tag{3.6}$$

It is numerically very inefficient to use Eq. (3.5), when Eq. (3.6) can in fact be solved analytically given the initial simplified conditions. We define X as the ratio between the thickness change due to flow and that due to evaporation rate,

$$x = \frac{2\rho\omega^2 h^3 / 3\eta}{\tilde{e}} \tag{3.7}$$

We then define a critical ratio x_c, at which the transition from the initial (Eq. (3.6)) to the intermediate stage (Eq. (3.5)) occurs. We define h_1 as the film thickness when the ratio $x = x_c$ in Eq. (3.7).

For a negligible evaporation rate, Eq. (3.6) can be solved analytically:

$$h = h_0(1 + \frac{4\rho\omega^2 h_0^{\,2}}{3} t)^{-1/2} \tag{3.8}$$

where h_0 is the initial thickness of the film. We can easily determine the time for the initial stage corresponding to thickness h_1. This time is typically about 1 s, much less than the experimental spin times employed. Use of this analytical formula reduces computational times by an order of magnitude. The choice of x_c does not strongly affect the observed relative variations of thickness with concentration, spin rate, or radius, but it does affect the magnitude of the thickness somewhat. In the simulations below, we chose x_c = 2 to best match the magnitude of the observed thicknesses.

In the intermediate stage, the viscosity, density, and evaporation rate of Eq. (5) become a function of the time dependent concentration. The change of concentration depends on evaporation and on the radial flow of solution if the concentration is different between neighboring points. When the polymer concentration is small, the evaporation rate is almost constant and thus the concentration at different positions is almost the same. When the PS

concentration becomes high, radial flow is greatly reduced, so that the change of concentration is dominated by evaporation, i.e., the concentration gradient and radial mass flow are together sufficiently small so that only evaporation need be accounted for in computing the local concentration. The validity of this approximation is confirmed by multiple simulations, as shown below.

For a nanocomposite solution, we again define the concentration of polymer as C_P (mg/ml), and the concentration of clay as C_C, and employ standard values for the density of solvent ρ_S, density of polymer ρ_P, and density of composite ρ_C. After a time increment Δt, the new concentrations of polymer $C_P^{'}$ and nanocomposite C_c' are:

$$C_P^{'} = \frac{C_P}{1-\frac{\tilde{e}\Delta t}{h}(1+\frac{C_P}{\rho_P}+\frac{C_C}{\rho_C})}$$
$$C_C^{'} = \frac{C_C}{1-\frac{\tilde{e}\Delta t}{h}(1+\frac{C_P}{\rho_P}+\frac{C_C}{\rho_C})} \quad (3.9)$$

Although the change of solution density is small and could be neglected, it is also straightforward to compute (assuming no volume change upon mixing) as:

$$\rho = \frac{\rho_s + C_p + C_c}{1+\frac{C_p}{\rho_p}+\frac{C_c}{\rho_c}} \quad (3.10)$$

Yonkoski and.Soane[95] have shown that the shear rate $\dot{\gamma}$ generated during spin coating should be:

$$\dot{\gamma}^2 = 2[(\frac{\partial V_r}{\partial r})^2 + (\frac{V_r}{r})^2 + (\frac{\partial V_z}{\partial z})^2] + (\frac{\partial V_r}{\partial z} + \frac{\partial V_z}{\partial r})^2 \qquad (3.11)$$

where the flow velocity has components in the radial and z directions of

$$V_r = \frac{\rho\omega^2 r}{\eta}(hz - z^2), \qquad V_z = -\frac{\rho\omega^2}{\eta}(hz^2 - \frac{1}{3}z^3) \qquad (3.12)$$

Inserting Eq. (3.12) into Eq. (3.11) yields a simple formula for the mean square shear rate $\dot{\gamma}^2$:

$$< \dot{\gamma}^2 >= \frac{\int_0^h \dot{\gamma}^2 dz}{h} = (\frac{\rho\omega^2 h}{\eta})^2 (\frac{6h^2}{5} + \frac{r^2}{3}) \qquad (3.13)$$

Thus, at each time interval, we can calculate the rms shear rate and concentrations. The shear rate is required in order to employ the measured viscosities of the previous section. The use of an rms shear rate is avoids the need for an intensive 3-D numerical simulation.

Eq. (3.5) can be written in the form of a difference equation as:

$$\Delta h = -[\frac{\rho\omega^2}{\eta}(\frac{r^2 h(r)^3 - (r-\Delta r)^2 h(r-\Delta r)^3}{r\Delta r}) + \tilde{e}]\Delta t \qquad (3.14)$$

Inserting the functions for viscosity and evaporation rate introduced in the experimental section, we can use numerical simulations to monitor the change in film thickness in the intermediate spinning stage.

After the spinner stops, the flow of the solution freezes. The remnant toluene in the film will continue to evaporate in still air, so that Eq. (3.5) becomes:

$$\frac{\partial h}{\partial t} = -\tilde{e}_0 \tag{3.15}$$

With this equation, it appears easy to simulate how the film thickness changes during the stage of film drying. However, the mathematical calculation is based on the assumption that the solution is incompressible. During this stage, the forces of gravity and adhesion may not be strong enough to compress the film. The free space left inside the film when the solvent evaporates is not accounted for in Eq. (3.15). Thus we can only approximately simulate the change of thickness during the film drying stage.

3.3.2 Amendment of the mass transfer model to include an orientation effect

In the present mass transfer model, as in previous models, the effect of shear thinning on the radial variation of film thickness is relatively small, as has been observed experimentally in a colloid system.[93] The large radial dependence of film thickness observed in the present study requires that the mass transfer model be amended to include the effect of platelet orientation. We connect the local platelet orientation to the calculated local shear rate, and maintain the simplicity and speed of the numerical simulation by employing a simple empirical equation. Though empirical, the amended model produces a reasonable fit to the radial dependence of film thickness as a function of both clay concentration and spin rate.

The degree of orientation can be described by the orientation order parameter[100]

$$S = < (3COS^2\delta - 1)/2 > \tag{3.16}$$

where δ is the deviation angle of the particle with respect to the flow direction. When all particles are aligned in the direction of flow, the parameter S is equal to 1, while for purely random orientation, S is equal to 0. Förster and his colleagues[100] have shown that, for an experimental system of cylindrical micelles, the viscosity is given by:

$$\eta = \eta_0 e^{-aS} \tag{3.17}$$

The parameter, a, has a value of ~13.8 over a wide range of micelle concentrations, and approaches 30 only at very high concentrations. In the Carreau Model, the zero shear viscosity η_0 is generally much larger than the infinite shear viscosity η_∞, so that we can make the approximation $\frac{\eta_\infty}{\eta_0} \approx 0$, and Eq. (3.1) can be simplified to:

$$\frac{\eta}{\eta_0} = (1 + \lambda^2 \dot{\gamma}^2)^{-N} \tag{3.18}$$

From equations (3.17) and (3.18), we derive:

$$S = \frac{N}{a} \ln(1 + \lambda^2 \dot{\gamma}^2) = \frac{N}{a} \ln(1 + \frac{\dot{\gamma}_m^{\,2}}{\dot{\gamma}_c^{\,2}}) \tag{3.19}$$

Here N is the slope of shear thinning curve, $\dot{\gamma}_m$ is the maximum shear rate during the entire spinning process, and $\dot{\gamma}_c$ is the shear thinning rate determined by experiment. Thus we are assuming that we can estimate the orientation order parameter from the experimental results for viscosity vs. shear rate.

The film, if free of voids, is composed of clay/polymer domains and free polymer. When Cloisite 6A exfoliates into the solvent, platelets with typical size 450 nm × 450 nm × 3.5 nm are produced. Polymer chains attach to both platelet surfaces and move with it, thus comprising a clay/polymer domain. The thickness of the domain, h_o, is on the order of the radius of gyration, and is approximated as 20 nm below. Randomly oriented domains extend over a vertical distance, h_r, on the order of (450 nm × 450 nm × h_o)$^{1/3}$ or 160 nm. For partial orientation, we employ a simple empirical formula to estimate the average vertical extent of a domain in the film:

$$h_S = h_o \times S + h_r \times (1 - S) \tag{3.20}$$

To estimate the number of domains stacked vertically, n, we first find the volume of clay contained in a film volume of dimensions 450 nm × 450 nm × h_c, where 450 nm is the mean platelet length and h_c is the film thickness calculated in the mass transfer model when shear flow ceases. (Shear flow is defined to cease when spinning terminates, or when the first term in Eq. (3.5) drops below 10^{-4} nm/s.) The parameter n is obtained by dividing this volume of clay by the volume of one clay platelet – 450 nm × 450 nm × 3.5 nm. In that region of the film, the "intrinsic" contribution to the film thickness, h_i, due to clay/polymer domains is defined to be $h_i = n\, h_S$.

During the process of simulation, we not only keep track of the concentrations at each location, but also of the maximum local shear rate. The maximum local shear rate determines the orientation parameter, S, in Eq. (3.19), and hence the intrinsic film thickness h_i. When shear flow ceases, the mass of clay and polymer at a given location is fixed, but solvent continues to evaporate. If the film thickness in the numerical simulation is observed to

drop below h_i, the thickness at the conclusion of the simulation is reported as h_i. In so doing, it is assumed that the clay/polymer domain orientations are fixed when shear flow freeze, and that additional solvent evaporation results in the presence of voids within the film.

3.4 Simulation Results and Discussion

The model was implemented in C++. The simulation results for the effect of clay concentration are shown in Fig 3-1; while those for the effect of spin rate are shown in Fig. 3-2. The solid lines in Figures 3-1 and 3-2 show the prediction of the model including the effect of platelet orientation, and provide a good fit to experiment. To compare the two models, normalized film thickness for spun cast PS /clay nanocomposite films were plotted in Fig. 3-10. The concentration of PS is 60mg/ml, clay concentrations vary as 0, 10, 20, 30, and 40 mg/ml. The spin rate is 2000rpm, spin time is 30 s, and the film was spun cast on as received silicon wafer. Experimental data appears in Fig. 3-10(a). The curves in Fig. 3-10(b) represent the normalized model predictions including the orientation effect. The calculated points in Fig. 3-10(c) correspond to the model prediction without the orientation effect, and

the inset reveals that these curves are not flat, but drop off by a few percent with distance from the rotation axis.

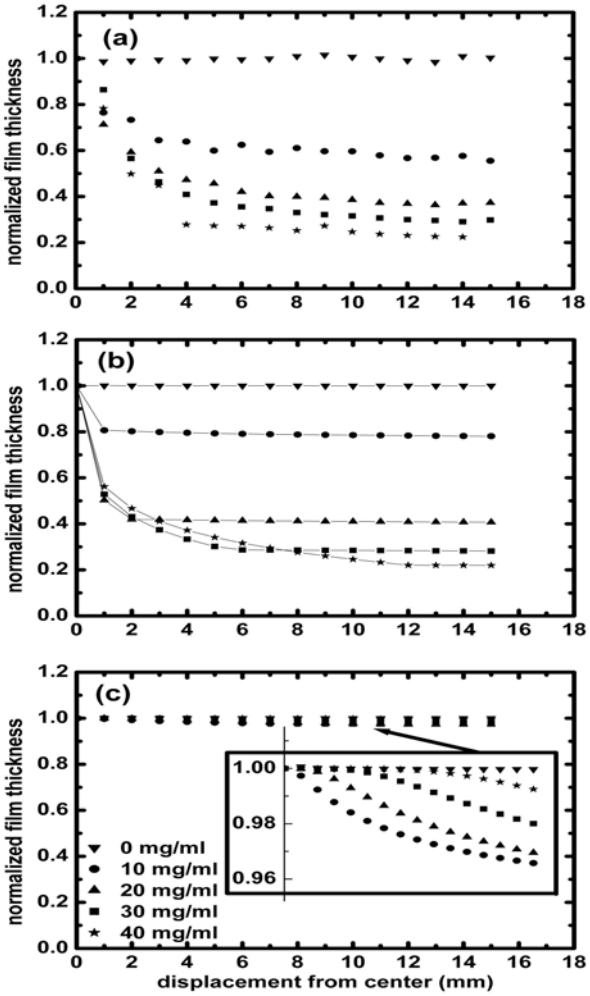

Fig. 3-10. Normalized film thickness vs. radius for spun cast PS/clay/toluene films on as received silicon wafer. PS concentration is 60 mg/ml, clay concentration is 40mg/ml, spin rate is 2000 rpm, spin time is 30s. (a) Measured data. (b) Model predictions including the effect of platelet orientation. (c) Model predictions without including the effect of orientation, and with a magnified view in the inset.

Britten and Thomas[93] examined colloidal suspensions of both spherical silica particles and elongated alumina particles. They observed no obvious film thickness variation for the silica sample, but a several percent variation for 300nm x 300nm x 50nm alumina particles. They employed a model similar to our mass transfer model to simulate their results, with an outcome similar to the results of Figure 3-10(c), but they did not account for the deviation between simulated and experimental results when the radius was small. The 50 nm thickness of their alumina particles is much larger than the thickness of Cloisite 6A platelets (3.5 nm), while the length of both particles were comparable. Therefore the orientation effect in their sample should be smaller, and indeed is only a few percent as compared to thickness variations of over 70% observed in our data.

3.5 Conclusion

The addition of Cloisite 6A clay particles to a PS/toluene solution increases the thickness of the resultant spin cast film. Films with clay show a strong radial dependence in film thickness, especially when the radius is small; the radial dependence is enhanced as clay concentration increases. The solutions with clay are highly non-Newtonian, i.e., they exhibit significant shear thinning. A computationally efficient mass transfer model was employed to calculate the film thickness, incorporating the effects of shear thinning. The model requires as input the shear dependent solution viscosity as a function of both polymer and clay concentration. The viscosity data for a wide range of concentrations were found to be well described by the Carreau model. Data for evaporation rate as a function of polymer and clay concentrations were also required, and were found to be well fit by a simple model equation.

At distances of several millimeters from the rotation axis, the mass transfer model performed well in describing both the magnitude of the film thickness and its variation with clay concentration and spin rate. In accord with previous studies, however, shear thinning produced a relatively small variation of film thickness in the mass transfer model. TEM cross sections reveal that the clay particles exfoliate efficiently in the film, and that the resulting clay platelets are randomly oriented near the center of rotation, but tend to align parallel to the wafer surface at larger distances from the center, due to strong shear. AFM and TEM both reveal that the platelets have a diameter on the order of 450 nm, a significant fraction of the film thickness. These results suggested that the mass transfer model should be amended to incorporate the effects of platelet orientation. The revised model correlates the degree of orientation with the maximum shear rate observed at a given location. The model furthermore assumes that the randomly oriented platelet/ polymer domains cannot collapse as the film dries. As a result, solvent evaporation should lead to the creation of voids in the film. The amended model does a much better job of describing the radial dependence of film thickness as a function of clay concentration and spin rate.

Chapter 4

EFFECT OF TEMPERATURE ON SHEAR INDUCED ANISOTROPIC STRUCTURE IN POLYMER CLAY HYDROGELS[2]

4.1 Introduction

Layered silicate based nanocomposite materials have attracted much recent interest, as they present a cost effective approach to improve the mechanical properties, flame retardance, and thermal stability of polymer systems.[1,120] The enhanced material properties not only depend on the dispersion of the filler, but also depend on the orientation of the high aspect ratio nanoparticles. Laponite RD, a synthetic clay, can disperse in water as disk–shaped particles, 30 nm in diameter and 1 nm in thickness. Each platelet displays more negative charge on its face, and less negative charge at the edge. The electrostatic interaction between platelets may lead to a house of cards structure described by van Olphan.[121] Clay platelets will orient under shear, and butterfly type patterning has been shown in light scattering experiments for colloids.[121]

Upon introduction of polymer to the clay aqueous solution, polymer chains will interact with the clay platelets and may be adsorbed to the surface of clay platelets. With contrast variation SANS measurement, Nelson and Cosgrove showed that the addition of PEO to a Laponite aqueous solution will cause the clay platelets to be enveloped by PEO, leading to a thickness change on each face of about 1.5 nm and a radius change in the range of 1.5 nm to 4.5 nm.[122]

---

[2] This chapter has been published at Macromolecular Rapid Communications 27, 1787 (2006)[119]

Under shear, the clay platelets may orient and thus stretch the polymer chains bridging the platelets; therefore an anisotropic shear induced structure can be expected. Schmidt and coworkers have observed the development of anisotropic neutron scattering and light scattering patterns for the PEO/Laponite aqueous solution under shear. [123,124] Shibayama et al. have observed that clay platelets are strongly tethered by Poly(N-isopropylacrylamide) (PNIPA) chains.[125] A butterfly SANS pattern develops when the sample is stretched. All these experiment have been performed at room temperature; the effect of temperature has not yet been revealed.

When temperature increases, the rotational Brownian motion of clay platelets acts in opposition to shear induced platelet orientation. Perrin[126] and Jerrard[127] showed that the rotational diffusion constant for platelet-like particles increases in proportion to temperature. At the same time, stretched polymer chains that bridge adjacent platelets will relax faster at higher temperature, again acting in opposition to shear induced anisotropy. In this regard, Doi and Edward[128] derived that the rotational relaxation time of polymer is inversely proportional to temperature. Temperature also affects PEO stability in aqueous solvent.[129-131] The attractive force between the PEO-covered surfaces in water has been predicted to be related to the temperature-dependent solubility of PEO in water.[129] As temperature increases, hydrogen bonds are more easily broken, decreasing the solvency of PEO in water, and consequently decreasing the layer thickness adsorbed to the particle.[130] At the same time, a higher temperature enhances the bridging interaction of polymer chains on adjacent particles,[131] which could aid the development of anisotropy. To elucidate the competing effects of stabilization, Brownian rotational motion, and relaxation, we examine here the evolution of shear induced structure in PEO LRD hydrogels at different temperatures.

4.2 Experiment

Samples were composed of 3.0 wt. % Laponite RD (LRD) (Southern Clay), Deuterium Oxide (D_2O) (99.7%, Cambridge), and 1.5 wt. % Poly(ethylene oxide) (PEO) (Aldrich) with Mw = 900,000 . LRD was added to D_2O and the solution was ultrasonicated for several hours and left still for about ten hours to assist the exfoliation of LRD. After the solution became transparent, PEO was added and the solution was magnetically stirred. It took about two weeks for the system to became homogeneous.

SANS experiments were performed at the NG3 and NG7 SANS instruments of the Center for Neutron Research, National Institute of Standards and Technology. The Boulder shear cell used in the dynamic SANS experiments has a Couette geometry with i.d. of 60.952 mm. The gap is 0.45 mm, giving a total path length of 0.90 mm through the sample. The incident neutron beam is parallel to the shear gradient. The incident wavelength, λ, was 6 Å and the scattering wave vector, q, covered range for the dynamic SANS experiments was 0.0029 $Å^{-1}$ to 0.0437 $Å^{-1}$. The temperature of the sample was set at 2^{o}C, 25^{o}C and 50^{o}C. At each temperature, the shear rate was increased from 0 s^{-1} to 1000 s^{-1} in 14 steps. Then the shear cell sat at rest to monitor the relaxation of the system. When the temperature was changed, a new sample was employed in order to avoid remnant shear effects. Static SANS was performed in the low q range (0.0021 $Å^{-1}$ to 0.0418 $Å^{-1}$) at temperatures of 10 ^{o}C, 20 ^{o}C, 30 ^{o}C, and 40 ^{o}C.

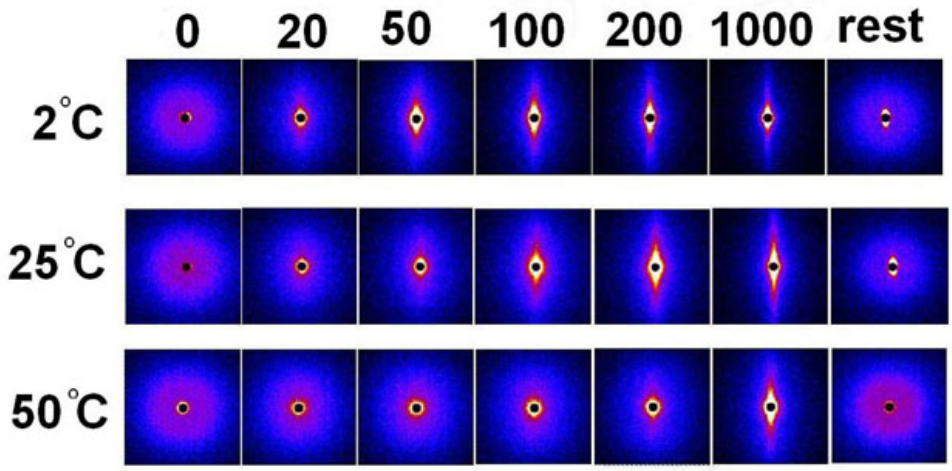

Fig. 4-1. Two dimensional SANS scattering patterns at three temperatures, with shear rates (s^{-1}). The patterns at the far right were obtained immediately after the application of highest shear, with the Couette cell at rest.

4.3. Results and Analysis

2D scattering patterns of dynamic SANS measurements at different temperatures and shear rates are shown in Fig 4-1. At 2 ^{o}C, anisotropy is apparent in the 2D image when the shear rate is 50 s^{-1}, while a similar pattern appears at 100 s^{-1} at 25 ^{o}C, and at 200 s^{-1} when the temperature is 50^{o}C. After the shear rate reached 1000 s^{-1}, the shear cell was stopped in order to monitor relaxation of the anisotropy. A scattering pattern was obtained at rest, as shown at the far right of the figure, within two minutes of cessation of motion.

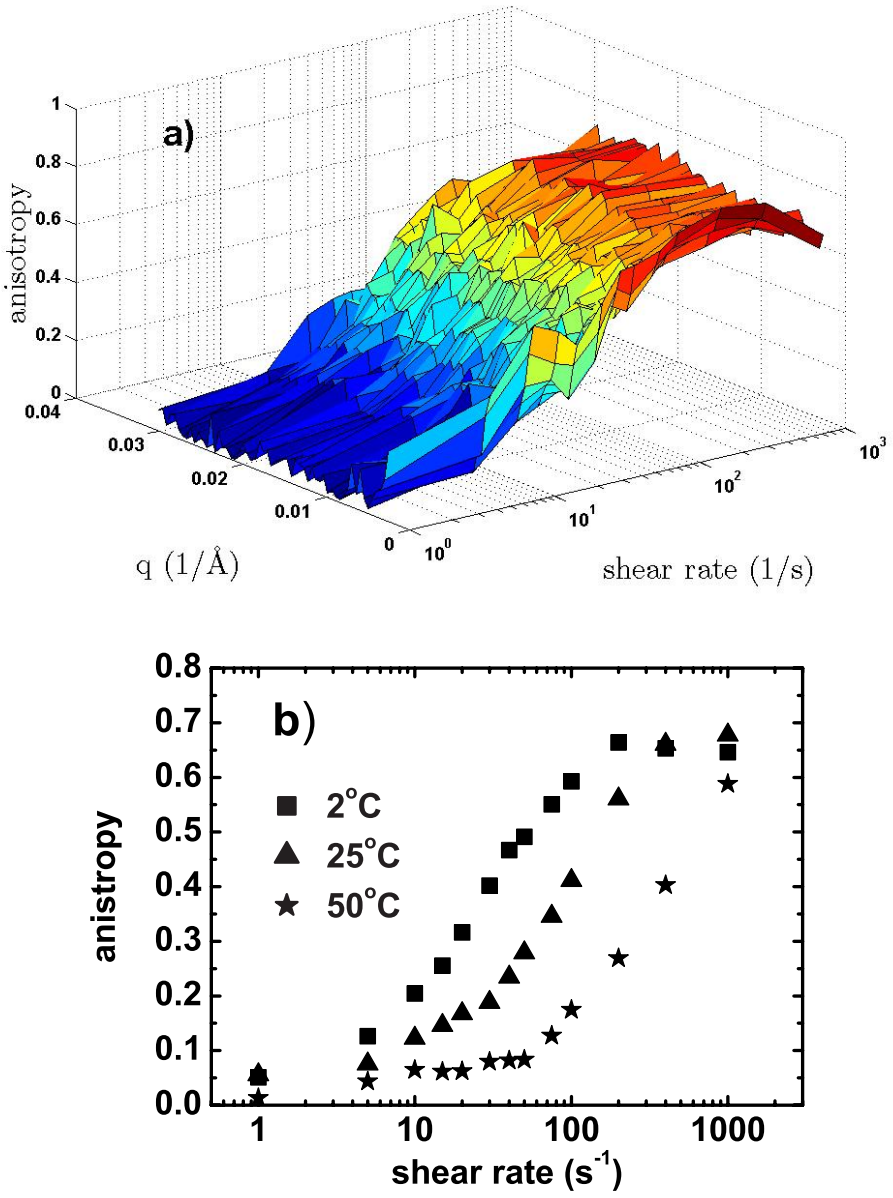

Fig 4 -2. a) SANS anisotropy |(Iy- Ix)/(Iy+Ix)| as a function of shear rate and q at 2°C b) Anisotropy averaged over the entire q range as a function of shear rate at three different temperatures as indicated.

At 2°C and 25°C, some anisotropy remains, while at 50 °C, the sample has become isotropic.

To elucidate the influence of temperature to anisotropy, we calculate the anisotropy |(Iy-Ix)/(Iy+Ix)| for different q at each shear rate. Ix and Iy corresponds to the SANS intensity from sectors around 0° (parallel to the flow) and 90° (perpendicular to the flow) in a range of 10 °, respectively. At 2 °C, the anisotropy as a function of q and shear rate is shown in Fig. 4-2 (a). The figure indicates that the change of the anisotropy is mainly dominated by the shear rate. Therefore the average anisotropies were calculated by integrating over the whole q range for each shear rate. As shown in Fig. 4-2 (b), anisotropy is more sensitive to shear rate as the temperature decreases. As noted previously, the anisotropic structure is generated by both the orientation of clay platelets and the stretch of polymer chains. At lower temperature, a smaller threshold shear rate is required to orient the clay platelets and stretch the polymer chains that bridge the clay platelets.

According to Hammouda et al., there exist two correlation lengths in the PEO/water system.[132] We also observed a drop off in the low q region of the SANS intensity curves. The curves can be well fit by the two correlation length Debye-Anderson-Brumberger (DAB) model:[133]

$$I = A_1/(1+q^2R_1^2)^2 + A_2\exp(-q^2R_2^2/4) \qquad (4.1)$$

where A_1 and A_2 are fitting parameters that depend on incident bean intensity and sample contrast, R_1 represents a short range correlation length, and R_2 represents the correlation length for a larger inhomogeneous region. The correlation function is:

$$\gamma(r) = f\exp(-r/R_1) + (1-f)\exp(-r^2/R_2^2) \tag{4.2}$$

where f is given by:

$$f = A_1 \Big/ [A_1 + \frac{8}{\sqrt{\pi}}(\frac{R_1}{R_2})^3 A_2] \tag{4.3}$$

Here *f* indicates the weight of short range correlation in the total correlation, so that 1-f represents the weight of long range correlation. When $f = 1$, the two correlation length DAB model reduces to the one correlation length DAB model.

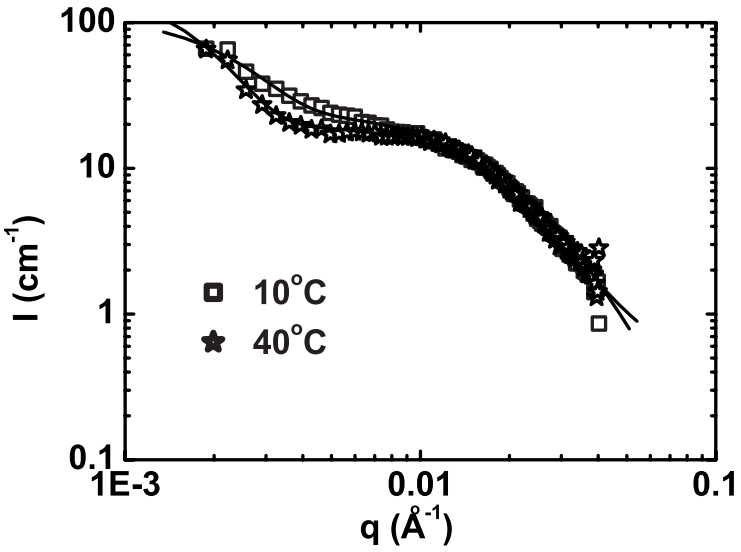

Fig. 4-3. Static SANS intensity vs. q at 10°C and 40°C. Solid lines show the fits obtained by the DAB model for the parameters given in Table 4-1.

Table 4-1. DAB fitting results for static SANS data

Temperature	R_1 (nm)	R_2 (nm)	1-f
10 °C	4.7	87	0.0025
20 °C	4.7	88	0.0022
30 °C	4.3	106	0.0015
40 °C	3.9	117	0.0014

We built a macro in Excel Solver and applied the two correlation length DAB model to fit the circular average static SANS data at different temperatures. Two of the fits are shown in Fig. 4-3. We clearly see a drop off near the low q end, indicating a long range correlation. The parameter values derived from the fits are shown in Table 4-1. As temperature increases from 10°C to 40 °C at zero shear, the short range correlation length drops from 4.7 nm to 3.9 nm, but the long range correlation length increases from about 87 nm to 117 nm. This is opposite to the trend observed in a pure PEO aqueous solution.[122] The relative weight of the long range correlation, 1 – f, decreases as temperature increases. It is likely that the short range correlation is associated with a domain composed of a clay platelet and adhered polymer, while the long range correlation represents the interaction between different domains. The short range correlation length of ~ 4 nm matches the thickness of clay platelet and polymer absorbed to it which has been observed by TEM [17], and also agrees with the thickness shown by Nelson and Cosgrove on a Laponite platelet wrapped by PEO.[122] On the other hand, the observed long range correlation length of ~100 nm is close to the mesh size in the hydrogel networks shown in

TEM[134], and is similar to the distance between polymer-covered clay rich domains observed by Small Angle X-ray Scattering (SAXS).[135]

The temperature dependence of the correlation lengths is consistent with the effects of steric repulsion and bridging interaction described by Shay and coworkers.[131] When temperature increases, solvency of PEO in water decreases, and grafted PEO chains shrink toward the particle surface. As the short range correlation length is associated with the thickness of the PEO/clay domain, it should therefore decrease at higher temperature. Furthermore, increased bridging interactions at higher temperature are likely related to the increase of the long range correlation length.

The influence of shear rate is revealed by applying the two correlation DAB model to the dynamic SANS data. As shown in Fig. 4-4(a) and 4-4(b), the short range correlation length is in the range of several nanometers. As shear rate increases, the short range correlation length tends to increase and the threshold shear rate is smaller at lower temperature. The increase of length may indicate shear extension of the polymer adhered to the clay platelets. At lower temperatures, a smaller energy is needed to deform the domain and therefore a smaller shear force is required to induce anisotropy.

As shown in Figure 4-4(c) and 4-4(d), the long range correlation length is in the range of 40 nm to 100 nm. In the x-direction, parallel to the direction of shear flow, this length drops rapidly from its static value, listed in Table 4-1, as shear is applied. The drop off with shear is slowest at 50 ^{o}C, as expected due to inhibition of platelet orientation by Brownian rotational motion at high temperature. In the perpendicular y-direction, only a small reduction in the long range correlation length is observed as shear is applied, consistent with a

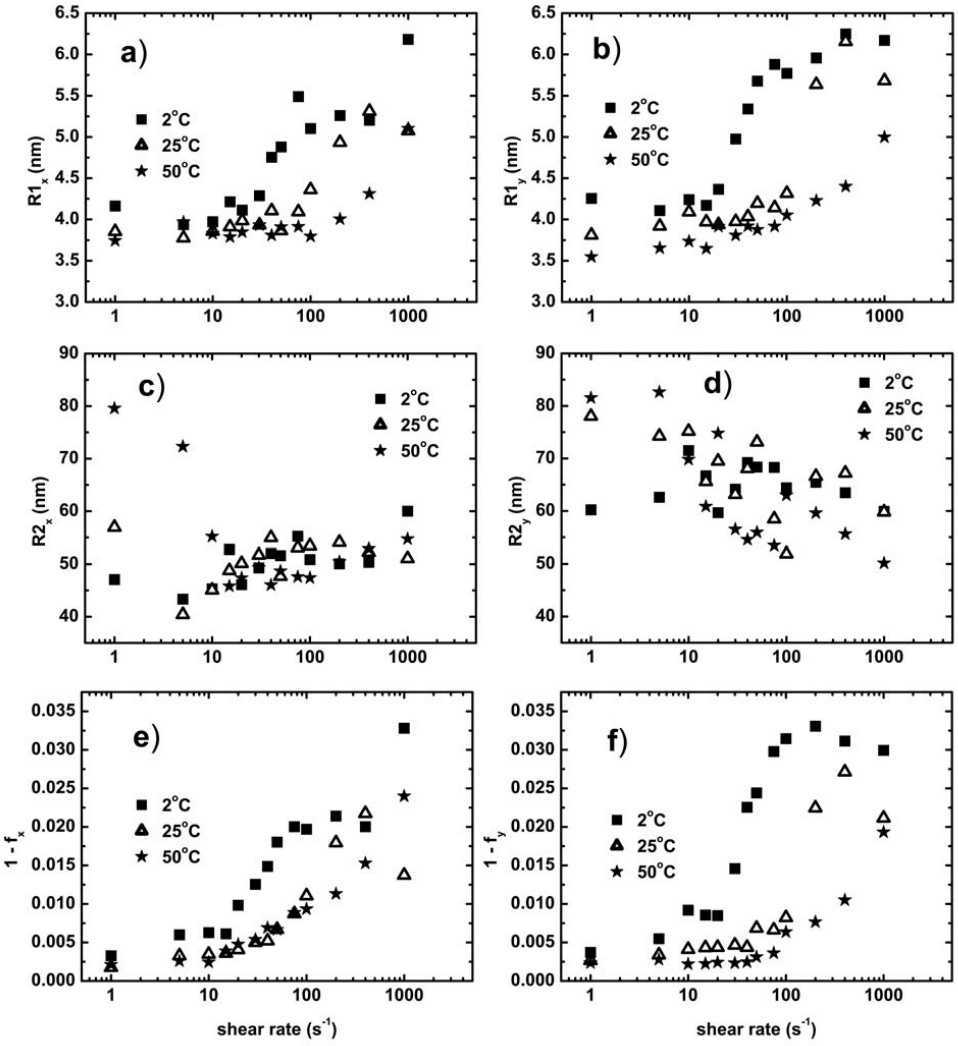

Fig. 4-4. Application of the DAB model to the dynamic SANS data averaged over a 10^{o} range in the X (parallel) and Y (perpendicular) directions. a) and b): Short range correlation lengths parallel and perpendicular to the shear flow direction; c) and d): Corresponding long range correlation lengths; e) and f): Corresponding relative strengths of long range correlation $1-f$.

small rotation of platelets in a direction perpendicular to shear flow. In Fig. 4-4 (e) and 4-4(f), the relative strength of long range correlation, *1-f,* increases as the shear rate rises. Furthermore, *1-f* begins to rise at a lower shear rate when temperature is lower. The presence of long range order is clearly correlated with the development of anisotropy, as evidenced by the similarity to the plot of anisotropy vs. shear rate in Fig. 4-2(b).

4.4 Conclusion

An application of the two correlation length DAB model to static and dynamic SANS data for the PEO/Laponite hydrogels at various temperatures reveals significant trends. The short correlation length, associated with polymer adhered to an individual platelet, decreases with temperature as attached PEO chains shrink towards the particle surface owing to decreased solubility. At zero shear, the long correlation length, associated with polymer chains bridging different clay platelets, increases with temperature while the strength of long range correlation decreases. The increased long correlation length is likely related to enhanced bridging interactions. As the shear rate increases, the short range correlation length increases, and is attributed to extension of adhered polymer chains. At low shear rate, the long range correlation length drops quickly with shear in the flow direction, especially at the lower temperatures, but is less affected in the perpendicular direction. As the shear rate increases, the long range correlation length in both directions hovers around 60 nm. However, the relative strength of long range correlation generally increases with shear rate, and is well correlated with the development of anisotropy at corresponding temperature, as observed in the SANS scattering patterns. These patterns also reveal rapid relaxation of

anisotropy at high temperature. Extension to other concentrations and molecular weights will be reported in a forthcoming publication.

receive additional instructions in the form of a sample thesis, press Ctrl-A to select all text. Choose AutoText twice from the Insert menu. Look in Thesis template, choose Gallery Example and click the Insert button. Choose Print from the File menu, and press Enter to receive a sample thesis with special instructions. After printing, re-open the thesis template, and follow the instructions of the printed sample.

Chapter 5

SHEAR RESPONSE IN POLYMER CLAY NANOCOMPOSITE HYDROGELS

5.1 Introduction

Polymeric hydrogels have attracted much attention as functional soft materials used in applications such as soft contact lens, super absorbent sanitary napkins and disposable diapers, carriers for protein and nucleic acid in gel electrophoresis, and support matrices for drug delivery and tissue replacement.[136-138] However polymeric hydrogels are weak and fragile because of the large proportion of water and the randomly cross-linked network structure. By introducing nanofillers into the system, we can make nanocomposite hydrogels which can overcome some of the limitations on mechanical properties of conventional polymeric hydrogels. Nanocomposite hydrogels show great potential as advanced soft materials in applications such as temperature-sensitive actuators and biocompatible materials.[138]

Laponite RD, synthetic clay, is a popular filler for nanocomposite hydrogels which has attracted much theoretical and application interest. It can disperse in water as disk–shaped particles, 25 nm in diameter and 1 nm in thickness. Each platelet displays more negative charge on its face, and less negative charge at the edge. The electrostatic interaction between platelets may lead to a house of cards structure described by van Olphan.[120] At low ionic strength, there exists a liquid-soft solid transition mainly driven by electrostatic repulsive interaction.[139] Harnau and coworkers have developed a reference interaction site model to describe the structure factor and phase transition of an aqueous suspension of clay.[140] Under shear, clay platelets will orient under shear, and

butterfly type patterning has been observed in light scattering experiments for clay gels.[121]

Upon introduction of polymer to the clay aqueous solution, polymer chains will interact with the clay platelets and may be adsorbed to the surface of clay platelets. With contrast variation SANS measurement, Nelson and Cosgrove showed that the addition of PEO to a Laponite aqueous solution will cause the clay platelets to be enveloped by PEO, leading to a thickness change on each face of about 1.5 nm and a radius change in the range of 1.5 nm to 4.5 nm.[122] If the polymer molecular weight is big enough, some polymer chains may bridge different clay platelets and draw them together. Swelson et al. demonstrated that equilibrium occurs between an entropy-driven drawing force, arising from partly stretched bridging polymers, and a bonding force to the clay platelets.[141] Under shear, the clay platelets may orient and thus stretch the polymer chains bridging the platelets; therefore an anisotropic shear induced structure can be expected. Schmidt and coworkers have observed the development of anisotropic neutron scattering and light scattering patterns for the PEO/Laponite aqueous solution under shear.[123,124] Shibayama et al. have observed that clay platelets are strongly tethered by Poly(N-isopropylacrylamide) (PNIPA) chains and a butterfly SANS pattern develops when the sample is stretched.[125]

We applied SANS to study the shear induced structure of the PEO/Laponite nanocomposite hydrogels. Then the SANS data was correlated with the rheology data to interpret the influence of clay and polymer clay concentration on the properties of the inside network. When we increase the clay concentration, if all the clay can still exfoliate, the average distance between two different clay platelets will decrease and thus make it easier for the

polymer to bridge platelets. With the clay concentration constant, the change of polymer concentration will lead to a competition between two effects. On one hand, the increase of polymer concentration will lead to more polymer chains bridging clay platelets and the stretch of those polymer chains under shear will make the SANS pattern anisotropic. On the other hand, if the polymer concentration is too high, each clay platelet will be saturated with polymer chains, thus a bigger portion of polymer may be free to move and this will keep the SANS pattern isotropic. Therefore we can predict that there exists an optimal ratio between clay and polymer concentration for the anisotropic SANS pattern to appear.

5.2 Experiment

Samples were composed of LRD (Southern Clay), Deuterium Oxide (D_2O) (99.7%, Cambridge), and PEO (99.5%, Aldrich) with Mw = 900,000, with concentrations shown in Table 1. LRD was added to D_2O and the solution was ultrasonicated for several hours and left still for about ten hours to assist the exfoliation of LRD. After the solution became transparent, PEO was added and the solution was magnetically stirred. It took about two weeks for the system to become homogeneous.

Table 5-1 Sample wt. concentration (%)

sample	LP0	LP1	LP2	LP3	LP4	LP5	LP6	LP7	LP8	LP9
PEO/D_2O	3	3	3	3	3	2	1.5	1	0.5	0
LRD/D_2O	0	1.5	2	2.5	3	3	3	3	3	3

SANS experiments were performed at the NG3 SANS instruments of the Center for Neutron Research, National Institute of Standards and Technology. The Boulder shear cell used in the dynamic SANS experiments has a Couette geometry with i.d. of 60.952 mm. The gap is 0.45 mm, giving a total path length of 0.90 mm through the sample. The incident neutron beam is parallel to the shear gradient. The incident wavelength, λ, was 6 Å and the scattering wave vector, q, range covered for the dynamic SANS experiments was 0.0029 $Å^{-1}$ to 0.0437 $Å^{-1}$. For each sample, the shear rate was increased from 0 s^{-1} to 1000 s^{-1} in 14 steps. Then the shear cell sat at rest to monitor the relaxation of the system. All the measurements were done at room temperature.

A TA ARES rheometer was applied in a dynamic frequency sweep from 0.01 rad/s to 100 rad/s with strain at 1% for all the samples at room temperature in the cone plate geometry. The cone and plate were stainless steel, with a cone diameter of 50 mm and cone angle of 2º. The plate diameter was 54 mm, 4 mm larger than the cone diameter to reduce edge effects. The plate had a lip at the perimeter to prevent material loss.

5.3 Results and Analysis

2D scattering patterns from SANS measurements for five samples under different shear rates are shown in Fig. 5-1. For sample LP1, as shown in series a, only when the shear rate has been increased to 1000 s^{-1} did a weak anisotropic pattern appear. But for sample LP4, whose LRD concentration is double that of LP1, we can see a clear anisotropic pattern at shear rate 200 s^{-1}. We further increase the concentration ratio between LRD and PEO by reducing PEO concentration. In series c, for sample LP6 whose PEO concentration is half that of LP1, the anisotropic pattern begins to appear at a

shear rate 50 s^{-1} and the SANS patterns become more anisotropic as the shear rate increases. However such a trend doesn't continue if we further reduce the PEO concentration. For sample LP7, as shown in series d, an anisotropic pattern also appears at a shear rate 50 s^{-1}, but it does not become as anisotropic as those for LP6 at higher shear rate. For sample LP8, we do not observe any anisotropic SANS pattern for the shear rates examined.

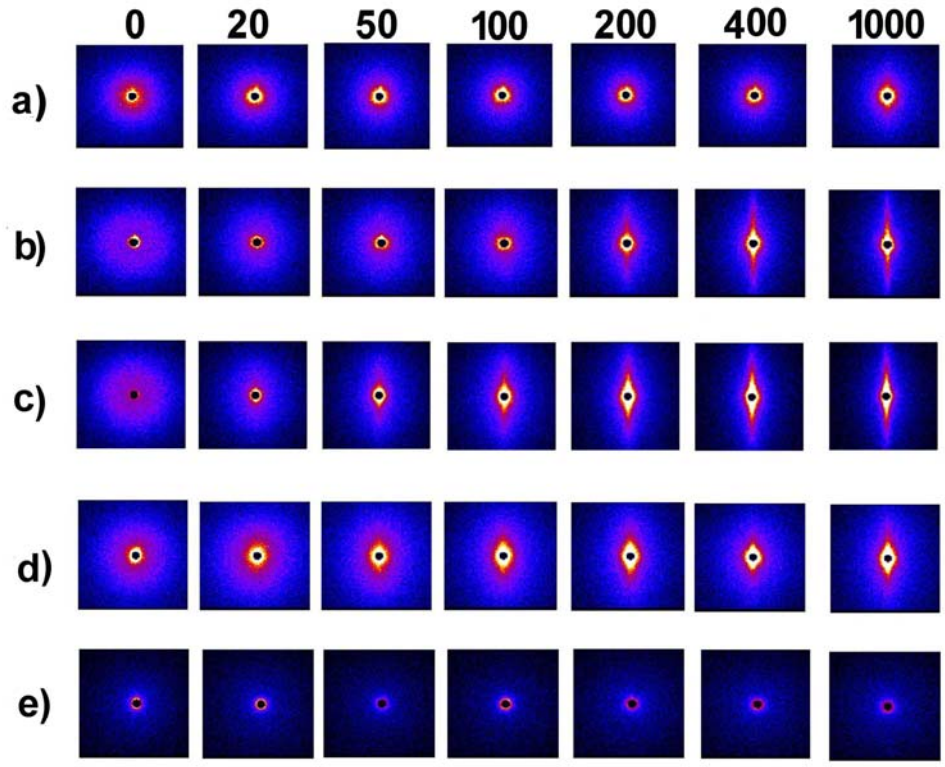

FIG.5-1. Two dimensional SANS scattering patterns for five samples under different shear rates (s^{-1}) as indicated above. a) LP1, b) LP4, c) LP6, d) LP7, e) LP8.

To elucidate the influence of concentration on anisotropy, we calculate the anisotropy $|(I_y-I_x)/(I_y+I_x)|$ for different q at each shear rate for different samples. I_x and I_y correspond to the SANS intensity from sectors around 0^o (parallel to the flow) and 90^o (perpendicular to the flow) in a range of 10^o, respectively. The average anisotropies were calculated by integrating over the whole q range for each shear rate. As shown in Fig. 5-2, anisotropy begins to increase at a lower shear rate and the value becomes bigger as the concentration ratio between LRD and PEO increases from 0.5 to 2. The trend disappears when the ratio is bigger than 2. According to the curve for sample LP7, whose concentration ratio is 3, the anisotropy increases with shear rate from 40 s^{-1} to 200 s^{-1}, but there is a big drop off when the shear rate reaches 400 s^{-1}. For sample LP8, whose concentration ratio is 6, the anisotropy stays around 0.

The source of the anisotropic SANS pattern mainly comes from two mechanisms: the orientation of clay platelets and the stretch of polymer chains bridging between clay platelets. In the hydrogel, some of the polymer chains remain independent of clay platelet, some may wrap the clay platelet, and some may bridge different platelets. When clay platelets orient, the independent polymer chains may not be strongly affected, but the bridged polymer chains may stretch and therefore generate anisotropic structure.

The higher the weight of bridged polymer chains, the more anisotropic is the shear induced structure. As the LRD/PEO concentration ratio increases, the weight of bridged polymers chains increases. But if the PEO concentration is too low, the total number of polymer chains bridging different clay platelets will be small. Thus they are not strong enough to endure a high shear rate and

some of the bridges may break; which can explain why the anisotropy for LP8 drops at 400 $s^{-1}$and the anisotropy for LP9 is almost always 0.

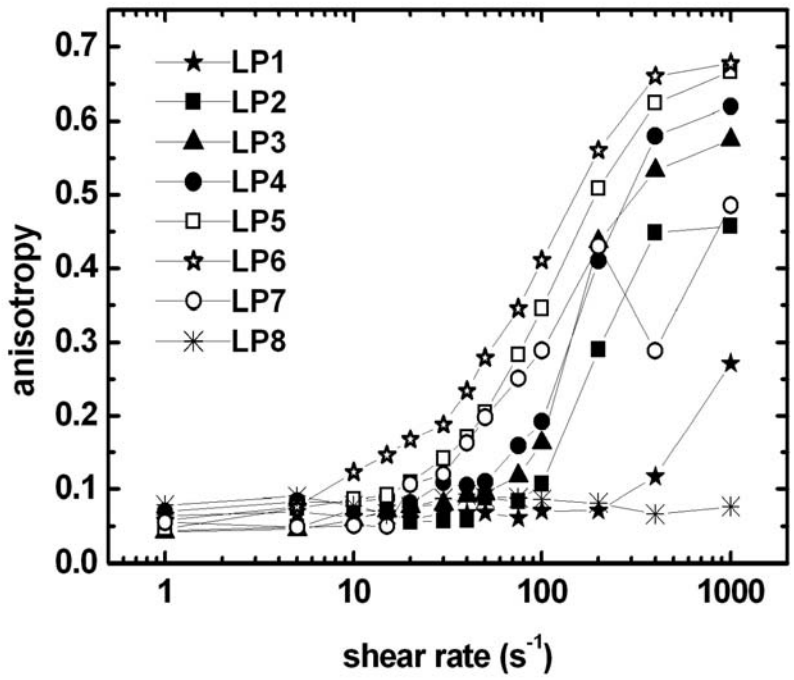

Fig. 5-2 Shear dependence of average SANS anisotropy $|(I_y-I_x)/(I_y+I_x)|$ over entire q range.

To further study the microstructure and the response to shear, we fit all the SANS data with a two correlation length Debye-Anderson-Brumberger (DAB) model:[133]

$$I = A_1/(1+q^2R_1^2)^2 + A_2\exp(-q^2R_2^2/4) \qquad (5.1)$$

where A_1 and A_2 are fitting parameters that depend on incident beam intensity and sample contrast, R_1 represents a short range correlation length, and R_2

represents the correlation length for a larger inhomogeneous region. The total correlation is:

$$\gamma(r) = f\exp(-r/R_1) + (1-f)\exp(-r^2/R_2{}^2) \tag{5.2}$$

where f is given by:

$$f = A_1 \Big/ [A_1 + \frac{8}{\sqrt{\pi}}(\frac{R_1}{R_2})^3 A_2] \tag{5.3}$$

Here *f* indicates the weight of short range correlation in the total correlation, so that 1-f represents the weight of long range correlation.

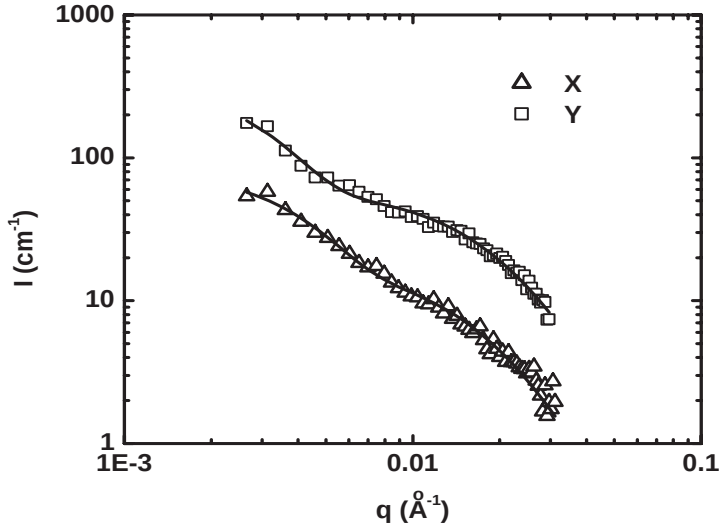

Fig. 5-3 SANS intensity curves for sample LP4 under shear rate 400 s^{-1}; averaged data along X and Y direction in a range of 10^o. Solid lines represent the prediction from the two correlation DAB model.

We apply the two correlation length DAB model to fit the section average SANS data in X and Y directions for samples under different shear rates. As shown in Fig. 5-3, this model provides a good fit to the SANS data of sample LP4 under shear rate 400 s^{-1}. To check the concentration effect on the microstructure inside the hydrogel, we fit the circular averaged SANS data of all samples under shear rate 0 s^{-1}. The derived short correlation lengths R_1 and their dependence on the PEO/LRD volume ratio is shown in Fig. 5-4(a). When the volume ratio is smaller than 3, R_1 is between 3 to 4 nm. This matches the thickness of clay platelet and polymer absorbed to it which has been observed by TEM,[134] and also agrees with the thickness shown by Nelson and Cosgrove on a Laponite platelet wrapped by PEO.[122] According to their work, the thickness of polymer layer and adsorbed polymer shows little variance with molecular weight. On the other hand, our work indicates that this thickness will change with volume ratio between polymer and clay. When the ratio is not large, polymer chains are adsorbed to the surface of the clay platelet and exist as one layer. Before the platelet face is saturated with polymer chains, the thickness don't vary much. After it is saturated, the layer will grow thicker as more polymer chains are adsorbed. That's why R_1 increases as the volume ratio rises above 3.

To further examine how the microstructure responds to shear, we fit the section average SANS data along X and Y directions for all samples under different shear rates. The fit result for sample LP1, LP4, and LP6 are shown in part (b), (c), (d) in Fig.5- 4 for R_1, R_2, and $1 - f$, respectively. As shown in Fig. 5-4(b), R_1 for LP4 and LP6 doesn't vary much at low shear rate, but it begins to increase with shear rate after some critical point. On the other hand, R_1 for sample LP1 which has a larger PEO/LRD volume ratio, decreases with shear rate in the low shear range. R_1 represents the thickness of the microdomain

composed of the clay platelet and polymer chains wrapping it. If the polymer clay volume ratio is high, then more polymer surrounds each platelet, and may

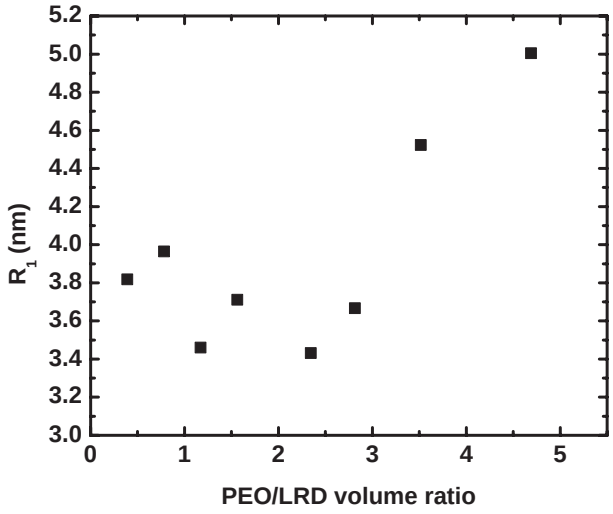

Fig. 5-4 Fits of the circular average intensity data at 0 shear rate with DAB model show an R1 dependence on polymer/clay volume ratio.

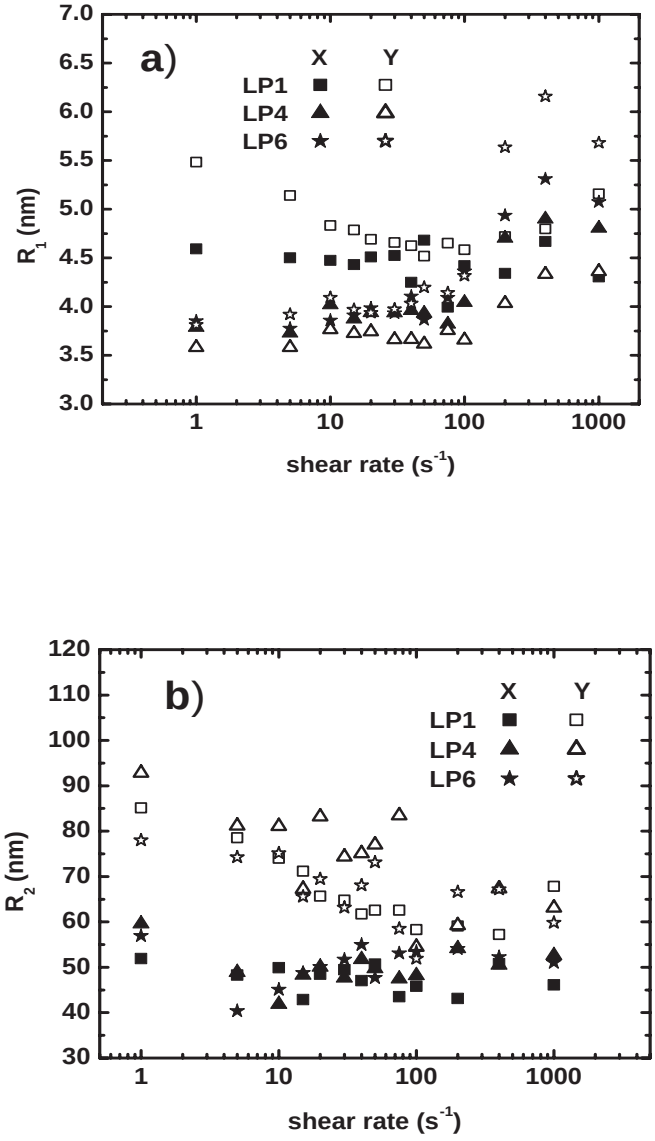

Fig. 5-5 Fits of the section average intensity data at different shear rates along X and Y directions, a) R1 dependence on shear rate; b) R2 dependence on shear rate.

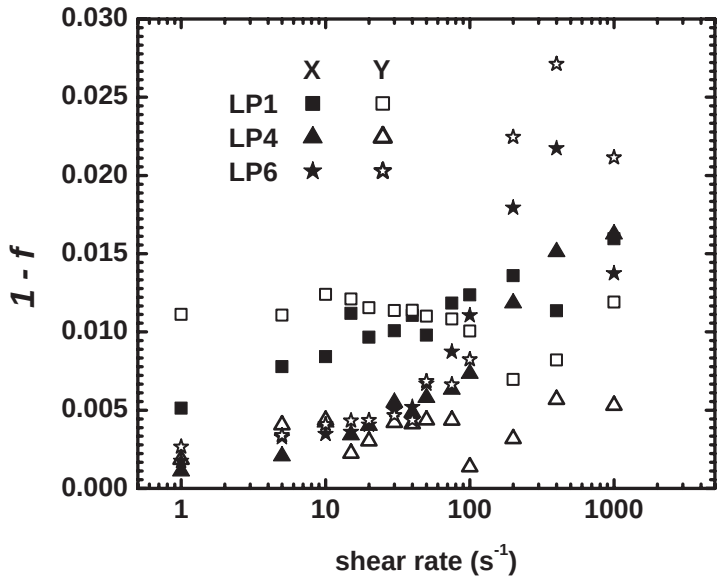

Fig. 5-6 Fits of the section average intensity data at different shear rates along X and Y directions showing the 1- f dependence on shear rate.

be compressed under shear; If this ratio is not high, the stretch effect under high shear rate will dominate and thus lead to the increase of R_1. From Fig. 5-4(c), we can tell that R_2 is generally bigger in the Y direction than the corresponding value in the X direction. R_2 represents the correlation length between different clay platelets and such correlation most likely comes from the polymer chains bridging platelets. Under shear, the clay platelet will begin to orient along the flow direction, X direction, and thus break some long bridging chains along that direction. Thus the long rang correlation length in the X direction will drop quikly at low shear rate. But this effect in the Y direction is not so strong, so the change for R_2 in the Y direction is not as fast

as that in X direction. As shear rate increases, the orientation of clay platelets is stronger and will disrupt some long distance polymer bridges. Eventually R_2 in both directions will fall to the same level. When clay platelets orient, they will also stretch the bridging polymers chains and will increase $1 - f$, the relative weight of long range correlation. In Fig. 5-4(d), we can see that $1 - f$ for samples LP4 and LP6 show obvious increases after a certain critical shear rate, but this trend is not so strong for sample LP1. In samples LP4 and LP6, the polymer chains have been stretched at high shear rate, which is revealed by the anisotropic SANS patterns shown in Fig. 5-1, but this effect is much weaker for sample LP1.

The change of microstructure is also reflected in the rheological properties of each sample. For the storage modulus, G', as shown in Fig.5-5 (a), we have observed two main behaviors when clay/polymer ratio increases: First, the value of G' increases with frequency until reaching a value around 1000 Pa; second, the slope of the curve decreases until it becomes almost flat. Samples LP6 and LP7, display the biggest storage modulus, G', and it is almost independent of frequency. This is especially clear for sample LP6. Comparing G' with the corresponding loss modulus, G'', as shown in Fig. 5-5 (b), we can see that G' is much bigger than G'' for these two samples. Therefore, we can say that these two samples are very elastic, and the networks inside the system are relatively intact. But we should also notice that there is a small dropoff in the G' curve for sample LP6 at frequency 0.05 rad/s, and for sample LP7 at frequency around 5 rad/s. This may be attributed to breaking of some bridging polymer chains.

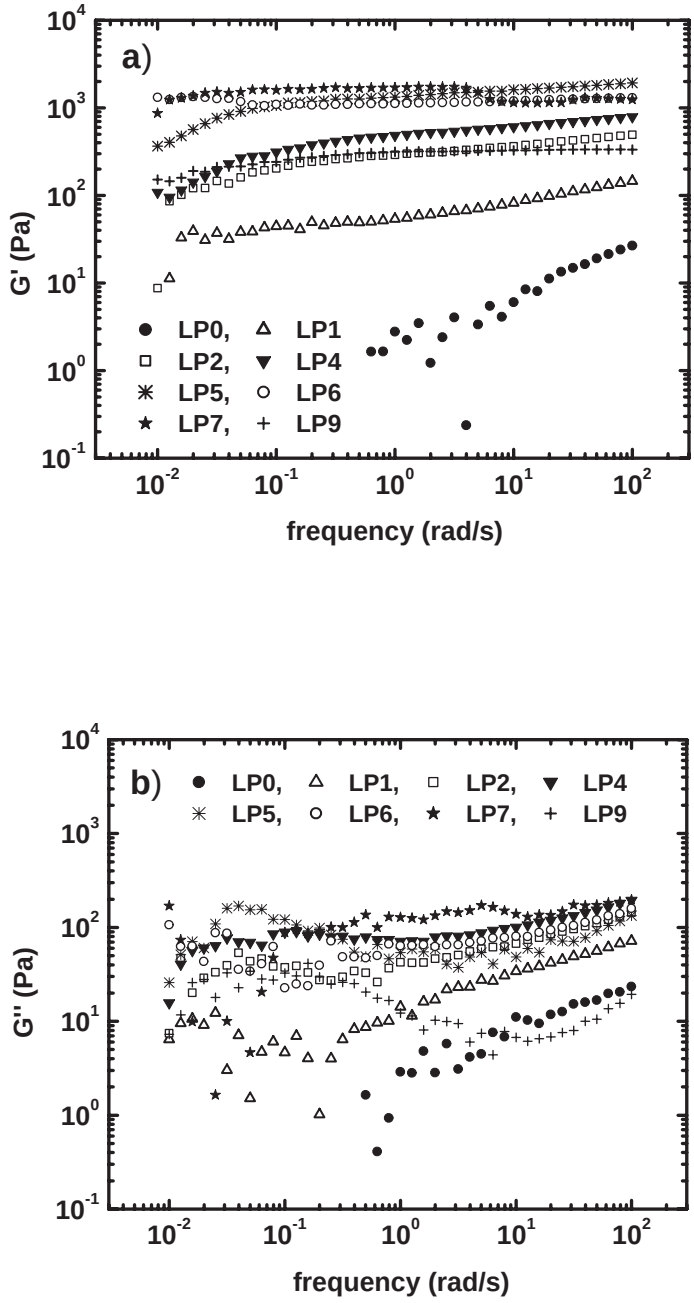

Fig. 5-7 Frequency response a)Elastic modulas, G'; b)Loss modulas, G".

5.4 Conclusion

In polymer clay nanocomposite hydrogels, as shown in Fig. 5-6, the polymer chains may exist in four conditions depending on their relationship to the clay platelets: 1. Much of the polymer chain length is absorbed to an individual clay platelets; 2. One part of the polymer chain is absorbed to one clay platelet, the other part is free from any platelets; 3. Polymer chains bridge two or more clay platelets; 4. The entire polymer chain is free from any platelet. When the polymer concentration is much smaller than the clay concentration, most polymer chains may exist in the first condition. As the polymer concentration increases, the quantity of the second kind of polymer chain will increase. If the end to end distance of the polymer chain is bigger than the average distance between clay platelets, more and more polymer chains will bridge different clay platelets. If the polymer concentration is too high, a lot of polymer chains may exist in the fourth condition. The quantity of the first two kinds of polymer chains may decide R_1, the thickness of the domains composed of the clay platelet and polymer attached to it. If the shear rate is greater than the critical shear rate, the domain size may change; for some samples R_1 increases with the shear rate. Under shear, the clay platelet will orient, and thus stretch the bridging polymer chains. First, the polymer chain bridging two clay platelets in the flow direction, X direction, may break and thus lead to the decrease of R_2 in that direction. As clay platelets orient more, this will also happen in Y direction. However, as the bridging polymer chains stretch, the interaction between different clay platelet will be stronger. So the relative weight of long range correlation, 1- f, will generally increase with the shear rate. As more and more bridging polymer chains stretch, the shear induced structure becomes more anisotropic. Because the first two kinds of polymer chains don't contribute to the anisotropic structure and the free polymer chains

will impede the development of anisotropic structure, it is easier to generate anisotropic structure if the bridging polymer chain is more prevalent. Thus the anisotropic SANS pattern will begin to appear under lower shear rate when the ratio between polymer and clay concentration is optimal. And in this case, the network will be relatively intact, and the system will be very elastic, so the elastic modulus will be much bigger than the loss modulus and will be almost independent of frequency.

Chapter 6

SUMMARY

The introduction of high aspect ratio nanofillers into a polymer matrix can form a nanocomposite material, which may lead to the improvement of some properties. The orientation of high aspect ratio nano fillers has an important effect on some specific properties of the material. We have studied the orientation effect of clay platelets in spin cast nanocomposite films. We also applied small angle neutron scattering to study shear induced clay orientation in nanocomposite hydrogels.

In the spin cast nanocomposite films project, we showed that there is strong radius dependence in the thickness of spin cast PS/Cloisite 6A/ toluene films. We first built a model based on mass transfer, which is similar to current models listed in the literature. This model numerically solves a hydrodynamic equation with shear viscosity and evaporation rate as input parameters. The instantaneous local shear viscosity during spinning is obtained from the dynamic fitting of the Carreau model. The evaporation rate is calculated based on a simple analytical model and supported by the experimental data. However this model failed to explain the strong radius dependence of the film thickness. We figured out that the orientation of clay platelets at different locations is a key reason for this. As the radius increases, the shear rate generated during spinning will increase and will lead more and more clay platelets to orientate parallel to the substrate. This was proved by the TEM for the cross sections of different parts of the spin cast nanocomposite films. The AFM of the surface also support this idea because it has been observed that the center part shows a higher roughness than the outer part due to the difference

of orientation. We further developed a numerical model which includes both the orientation effect and hydrodynamic effect. This model provides a good fit to the experimental data over a wide range of spin parameters.

In this project, the molecular weight of the PS used is 280K. We have also examined the system composed of different molecular weights. The experimental data show that the change of molecular weight will lead to the change to both shear thinning curve viscosity and local thickness distribution. However we have not extended the model to any molecular weight system, this needs further research work. On the other hand, we use Cloisite 6A as nanofillers in the system. Cloisite 6A can exfoliate into toluene as platelets, with an aspect ratio around 100. If we introduce different aspect ratio nanofillers into the system, we may observe the orientation effect to a different degree. Furthermore, different shapes of nanofillers such as nanobar or nanotube may lead to a big difference in orientation effect. The exact detail need further study.

In the nanocomposite gel project, we have applied small angle neutron scattering to study the shear induced clay orientation in PEO/Laponite RD nanocomposite hydrogels. Furthermore, we applied a two correlation length DAB model to fit the SANS data. The fitting result gave us two correlation lengths, a short range correlation length and long range correlation length. The short range correlation length is about 5 nm, which is likely to be the thickness of a domain composed of a clay platelet and polymer chains wrapping it. The long range correlation length is about 50 nm, which is likely to be the distance between two clay platelets. Under shear, the clay platelets begin to orient along the flow direction and may stretch bridging polymer chains. This will change both the short range correlation length and long range correlation

length. The detail of the change will depend on temperature, concentration and molecular weight of polymer.

We have shown that temperature will affect the shear orientation from several aspects. First, the increase of temperature will lead to a stronger rotational Brownian motion and will impede the orientation of the clay platelets. Second, a higher temperature will cause the stretched polymer chains to relax faster, thus the anisotropic scattering patterns will disappear faster. Last but not least, the temperature will affect the stabilization of PEO in water and thus lead to a change of microstructure in the gel.

We have also demonstrated that an optimal PEO Laponite RD concentration may lead to an anisotropic SANS pattern. Based on the fitting results of the two correlation length DAB model and the rheology data, we deduced that an elastic structure can develop inside the gel if the concentration of PEO and Laponite RD is proper. In this case, the elastic modulus, G', is much bigger than the loss modulus, G'', and is almost independent of frequency.

We have even collected a lot of SANS data to study the effect of molecular weight. The experimental results showed that a higher molecular weight may lead to anisotropic structure at a lower temperature. Furthermore, there is a critical molecular weight to generate anisotropic SANS patterns. The effect of molecular weight may be explained from the point view of polymer bridges. However, we have not finished this work yet. In the future, we will develop a probabilistic model to simulate the network evolution inside the nanocomposite gels. This model should be able to give a numerical explanation to all SANS data we have collected.

BIBLIOGRAPHY

1. M. Alexandre and P.Dubios, Material Science and Engineering **28**, 1 (2000)

2. Y. Sun and Y. Xia, Science **298**, 2176 (2002)

3. T. Kalkbrenner, U. Håkanson, A. Schädle, S. Burger, C. Henkel, and V. Sandoghdar1, Phys. Rev. Lett. **95**, 200801 (2005)

4. M. Ishifuji, M. Mitsuishi,_ and T. Miyashita, Appl. Phys. Lett. **89**, 011903 (2006)

5. D. M. Schaadt, B. Feng, and E. T. Yu, Appl. Phys. Lett. **86**, 063106 (2005)

6. J. H. Park, Y. T. Lim, O O. Park, J. K. Kim, J.W. Yu, and Y. C. Kim, Chem. Mater. **16**, 688 (2004)

7. D. I. Gittins, D. Bethell, D. J. Schiffrin and R. J. Nichols, Nature **408**, 67 (2000)

8.I. E. Protsenko, A. V. Uskov, O. A. Zaimidoroga, V. N. Samoilov, and E. P. O'Reilly, Phys. Rev. A **71**, 063812 (2005)

9. R. K. Zheng, H. Gu, B. Xu, and X. X. Zhang, Phys. Rev. B **72**, 014416 (2005)

10. K. F. MacDonald, V. A. Fedotov, and N. I. Zheludev, Appl. Phys. Lett. **82**, 1087 (2003)

11. N. B. Shevchenko, J. A. Christodoulides, and G. C. Hadjipanayis, Appl. Phys. Lett. **74**, 1478 (1999)

12. S. Sun, C. B. Murray, D. Weller, L. Folks, A. Moser, Science **287**, 1989 (2000)

13. H. Zeng, J. Li, J. P. Liu, Z. L. Wang, and S. Sun, Nature **420**, 395 (2002)

14. A. C. C. Yu, M. Mizuno, Y. Sasaki, H. Kondo, and K. Hiraga Appl. Phys. Lett. **81**, 3768 (2002)

15. S. A. Majetich and Y. Jin, Science **284**, 470 (1999)

16. R. Lopez, L. C. Feldman,† and R. F. Haglund, Jr., Phys. Rev. Lett. **93**, 177403 (2004)

17. R. N. Bhowmik, R. Nagarajan, and R. Ranganathan1, Phys. Rev. B **69**, 054430 (2004)

18. Y. Jeon, G. H. Lee, J. Park, B. Kim, Y. Chang, J. Phys. Chem. B **109**, 12257 (2005)

19. A. Murali, A. Barve, V. J. Leppert, S. H. Risbud. I. M. Kennedy, and H. W. H. Lee, Nano Lett. **1** ,287 (2001)

20. D. Son, E. Kim, T. Kim, M. G. Kim, J. Cho, and B. Park, Appl. Phys. Lett. **85** 5875 (2004)

21. B. Sun, E. Marx, and N. C. Greenham, Nano Lett. **3,** 961 (2003)

22. Y. Tomita, K. Furushima, K. Ochi, K. Ishizu, A. Tanaka, M. Ozawa, M. Hidaka, and K. Chikama, Appl. Phys. Lett. **88**, 071103 (2006)

23. B. K. An, S. K. Kwon, S. D. Jung, and S. Y. Park, J. AM. CHEM. SOC. **124**, 14410 (2002)

24. S. Kolliopoulou, P. Dimitrakis, P. Normand , H. L. Zhang, N. Cant, S. D. Evans, S. Paul, C. Pearson, A. Molloy, ,M. C. Petty, and D. Tsoukalas, J. Appl. Phys. **94**, 5234 (2003)

25. T. W. Ebbesen, Annu. Rev. Mater. Sci. **24**, 235 (1994)

26. T.W. Ebbesen and P. M. Ajayan, Nature **358**, 683 (1992)

27. D. S. Bethune, C. H. Kiang, M.C. de Vires, G. Gorman, R. Savoy, J. Vazquez, and R. Beyers, Nature **363**, 605 (1993)

28. S. Iijima and T. Ichihashi, Nature **363**, 603 (1993)

29. S. Iijima, Nature **354**, 56 (1991)

30. R. Martel, T. Schmidt, H. R. Shea, T. Hertel, and Ph. Avouris,Appl. Phys. Lett.**73**, 2447 (1998)

31. H. W. Ch. Postma, T. Teepen, Z. Yao, M. Grifoni, and C. Dekker, Science **293**, 76 (2001)

32. K. Balasubramanian, R. Sordan, M. Burghard, and K. Kern, Nano Lett. **4**, 827 (2004)

33. A. Javey, H. Kim, M. Brink, Q. Wang, A. Ural, J. Guo, P. Mcintyre, P. Mceuen, M. Lundstrom, and H. J. Dai, Nature Materials **1,** 241 (2002)

34. A. Bachtold, P. Hadley, T. Nakanishi, C. Dekker, Science **294** 1317 (2001)

35. H. T. Soh, C. F. Quate, A. F. Morpurgo, C. M. Marcus, J. Kong, and H.J. Dai, Appl. Phys. Lett. **75**, 627 (1999)

36. Q. H. Wang, A. A. Setlur, J. M. Lauerhaas, J. Y. Dai, E. W. Seelig, and R. P. H. Chang, Appl. Phys. Lett. **72**, 2912 (1998)

37. W. B. Choi, D. S. Chung, J. H. Kang, H. Y. Kim, Y. W. Jin, I. T. Han, Y. H. Lee, J. E. Jung, N. S. Lee, G. S. Park, and J. M. Kim, Appl. Phys. Lett. **75**, 3129 (1999)

38. J. Kong, N. R. Franklin, C. Zhou, M. G. Chapline, S. Peng, K. Cho, H. Dai, Science **287**, 622 (2000)

39. J. Wang, Electroanalysis **17**, 7 (2005)

40. A. C. Dillon, K. M. Jones, T. A. Bekkedahl, C. H. Kiang, D. S. Bethune, and M. J. Heben, Nature **386**, 377 (1997)

41. G. Che, B. B. Lakshmi, E. R. Fisher, and C. R. Martin, Nature **393**, 346 (1998)

42. C. Li and T. W. Chou, Phys. Rev. B **68**, 073405 (2003)

43. R. H. Baughman, C. Cui, A. A. Zakhidov, Z. Iqbal, J. N. Barisci, G. M. Spinks, G. G. Wallace, A. Mazzoldi, D. De Rossi, A. G. Rinzler, O. Jaschinski, S. Roth, and M. Kertesz, Science **284**, 1340 (1999)

44. R. K. Rana, X. N. Xu, Y. Yeshurun, and A. Gedanken *J.* Phys. Chem. B **106**, 4079(2002)

45. R. S. Lee, H. J. Kim, J. E. Fischer, A. Thess, and R. E. Smalley, Nature **388**, 255 (1997)

46. G. P. Siddons, D. Merchin, J. H. Back, J. K. Jeong, and M. Shim, Nano Lett. 4 ,927 (2004)

47. G. W. Webb, Appl. Phys. Lett. **59**, 3393 (1991)

48. X. Zong, K. Kim, D. Fang, S. Ran, B. S. Hsiao, and B. Chu, Polymer **43**, 4403 (2002)

49. H. Yoshimoto, Y. M. Shin, H. Terai, and J. P. Vacanti, Biomaterials **24**, 2077 (2003)

50. X. M. Mo, C. Y. Xu, M. Kotaki, and S. Ramakrishna, Biomaterials **25,** 1883 (2004)

51. K. Lozano and E. V. Barrera, J. Appl. Polym. Sci. **79**, 125 (2000)

52. E. S. Steigerwalt, G. A. Deluga, D. E. Cliffel, and C. M. Lukehart, J. Phys. Chem. B **105**, 8097 (2001)

53. C. X. Xu, X. W. Sun, and B. J. Chen, Appl. Phys. Lett. **84**, 1540 (2004)

54. A. Chambers, T. Nemes, N. M. Rodriguez, and R. T. K. Baker, J. Phys. Chem. B **102**, 2251 (1998)

55. S. Virji, J. Huang, R. B. Kaner, and B. H. Weiller, Nano Lett. **4**, 491 (2004)

56. G. Gu, M. Schmid, P. W. Chiu, A. Minett, J. Fraysse, G. T. Kim, S. Roth, M. Kozlov, E. Muñoz, and R. H. Baughman, Nature Materials **2**, 316 (2003)

57. J. J. Urban, W. S. Yun, Q. Gu, and H. Park, J. AM. CHEM. SOC. **124**, 1186 (2002)

58. Y. W. Jun, S. M. Lee, N. J. Kang, and J. Cheon,J. Am. Chem. Soc. **123** , 5150 (2001)

59. V. M. Cepak and C. R. Martin, J. Phys. Chem. B **102**, 9985 (1998)

60. W. U. Huynh, J. J. Dittmer, N. Teclemariam, D. J. Milliron, and A. Paul Alivisatos, Phys. Rev. B **67**, 115326 (2003)

61. H. M. Kim, Y. H. Cho, H. Lee, S. Il Kim, S. R. Ryu, D. Y. Kim, T. W. Kang, and K. S. Chung, Nano Lett. **4**,1059 (2004)

62. W. U. Huynh, J. J. Dittmer, A. P. Alivisatos, Science **295**, 2425 (2002)

63. S. A. Solin, Annu. Rev. Mater. Sci. **27**, 89(1997)

64. E. P. Giannelis, R. Krishnamoorti , and E. Manias , Adv. Polym. Sci. **118**, 108 (1999)

65. S. S. Ray and M. Okamoto, Progress in Polymer Science **28**, 1539 (2003)

66. T. J. Pinnavaia, Science **220**, 365, (1983)

67. M. Biswas and S. S. Ray, Polymer **39**, 6423 (1998)

68. J. W. Kim, S.G. Kim, H. J. Choi, M. S. Jhon, Macromol Rapid Commun 20, 450 (1999)

69. C. Oriakhi, Chem. Br. **34**, 59 (1998).

70. O. C. Wilson Jr., T. Olorunyolemi, A. Jaworski, L. Borum, D. Young, A. Siriwat, E. Dickens, C. Oriakhi, M. Lerner, Appl. Clay Sci. **15**, 265(1999)

71. C.O. Oriakhi, I.V. Farr, M.M. Lerner, Clays and Clay Minerals **45**, 194 (1997).

72. R. Krishnamoorti and E. P. Giannelis, Macromolecules **30**, 4097 (1997)

73. Y. H. Hyun, S. T. Lim, H. J. Choi, and M. S. Jhon, Macromolecules **34**, 8084 (2001)

74. T. H. Kim, L. W. Jang, D. C. Lee, H. J. Choi, and M.. S. Jhon, Macromol. Rapid Commun **23**, 191 (2002)

75. M. A. Osman, V. Mittal, M. Morbidelli, and U. W. Suter, Macromolecules **36**, 9851 (2003)

76. J. W. Gilman, C. L. Jackson, A. B. Morgan, R. Harris, Jr., E. Manias, E. P. Giannelis, M. Wuthenow, D. Hilton and S. H. Phillips, Chem. Mater.**12**, 1866 (2000)

77. S. R. Lee, H. M. Park, H. Lim, T. Kang, X. Li, W. J. Cho, and C.S. Ha, Polymer **43**, 2495 (2002)

78. C. L. Lin and T. J. Pinnavaia, Chem. Mater. 3, 213(1991)

79. J. Feng, X. Hu, and P. Yue, Environ. Sci. Technol. **38**, 269(2004)

80. Y. P. Huang1, H. Y. Chen, W. Lee, T.Y. Tsai and W. K. Chin Nanotechnology **16**, 590 (2005)

81. H.J. Walls , M.W. Riley , R.R. Singhal , R.J. Spontak , P.S. Fedkiw , and S.A. Khan, Advanced Functional Materials **13**, 710 (2003)

82. D. Margarita, C. Montserrat, R. H. Eduardo, and B. M. Franca, Applied Clay Science **28**, 199 (2005)

83. M.Y. Lin, Lecture note: Scattering Techniques in Studying Complex Fluids and Porous Media.

84. F. Horkay, A.Marie, and E. Geissler, Macromolecules **31**, 8851(1998)

85. P. J. Flory, Principles of Polymer Chemistry; Cornell University Press: Ithaca, NY, 1953.

86. P.G. de Gennes, Scaling Concepts in Polymer Physics; Cornell University Press: Ithaca, NY, 1979.

87. J. D. Ferry, Viscoelastic Properties of Polymers; Wiley: New York, 1980.

88. F. Horkay, A. M. Hecht, S. Mallam, E. Geissler, and A. R. Rennie, Macromolecules **24**, 2896(1991)

89. J. Li, S. A. Schwarz, Y. Ji, M. H. Rafailovich, J. Sokolov, G. Rudomen, and W. H. Feng, Appl. Phys. Lett. **89**, 111917 (2006)

90. D. B. Mitzi, L. L. Kosbar, C. E. Murray, M. Copel, and A.Afzali, Nature **428**, 299 (2004); A. Singh, and M. Mukherjee, Phys. Rev. E **70**, 051608 (2004)

91. T. C. Merkel, Z. He, I. Pinnau, B. D. Freeman, P. Meakin, and A. J. Hill, Macromol. **36**, 6844(2003)

92. S. A. Jenekhe and S. B. Schuldt, Ind. Eng. Chem. Fundam. **23**, 432 (1984)

93. J. A. Britten and I. M. Thomas, J. Appl. Phys. **71**, 972 (1992)

94. Y. T. Lim and O. O. Park, Macromol. Rapid Comm. **21**, 231(2000)

95. R. K. Yonkoski and D. S. Soane, J. Appl. Phys. **72**, 725 (1992)

96. P. J. Carreau, Journal of Rheology **16**, 99 (1972)

97. F. Kreith, J. H. Taylor and J. P.Chong, J. Heat Transfer, May, 95 (1959)

98. D. E. Haas, J. N. Quijada, Sol-Gel Optics V, in SPIE Proc. **280**, 3943 (2000)

99. D. B. Hall, P. Underhill, and J. M. Torkelson, Polym. Eng. Sci. **38**, 2039 (1998)

100. Főrster, M. Konrad, and P. Lindner, Phys. Rev. Lett. **94**, 017803 (2005)

101. D. V. Talapin and C. B. Murray, Science **310**, 86 (2005).

102. H. Wang, C. C. Oey, A. B. Djurisic, M. H. Xie, Y. H. Leung, K.K. Y. Man, W. K. Chan, A. Pandey, J. M. Nunzi, and P. C. Chui, Appl. Phys. Lett. **87**, 023507 (2005).

103. X. Yang, J.K.J. van Duren, M. T. Rispers, J. C. Hummelen, R.A.J. Jassen, M.A.J. Michels, and J. Loos, Adv. Mater. **16**, 802 (2004).

104. N. Tessler, V. Medvedev, M. Kazes, S. Kan, and U. Banin, Science 295, 1506 (2002).

105. J. S. Kim, R. H. Friend, I. Grizzi, and J. H. Burroughes, Appl. Phys. Lett. 87, 023506 (2005).

106. G. D. Stucky, Nature 410, 885 (2001).

107. A. G. Emslie, F. T. Bonner, and L. G. Peck, J. Appl. Phys. 29, 858 (1958).

108. A. Acrivos and M. J. Shah, and E.E.Petersen ,J. Appl. Phys. **31**, 963 (1960)

109. D. Meyerhofer, J. Appl. Phys. **49**, 3993 (1978).

110. W. W. Flack, D. S. Soong, A. T. Bell, and D. W. Hess, J. Appl. Phys. **56**, 1199 (1984).

111. C. J. Lawrence, Phys. Fluids **31**, 2786 (1988).

112. D. E. Bornside, C. W. Macosko, and L. E. Scriven, J. Appl. Phys. **66**, 5185 (1989).

113. T. Ohara, Y. Matsumoto, and H. Ohashi, Phys. Fluids A **1**, 1949 (1989).

114. A. Oron, S. H. Davis, and S. G. Bankoff, Rev. Mod. Phys. **69**, 931 (1997).

115. A. Kitamura, Phys. Fluids **13**, 2788 (2001).

116. M. Y. Gelfer, C. Burger, B. Chu, B. S. Hsiao, A. D. Drozdov, M. Si, M. Rafailovich, B. B. Sauer, and J. W. Gilman, Macromolecules **38**, 3765 (2005).

117. T. C. Merkel, Z. He, I. Pinnau, B. D. Freeman, P. Meakin, and A. J. Hill, Macromolecules **36**, 6844 (2003).

118. M. A. Osman, V. Mittal, M. Morbidelli, and U. W. Suter, Macromolecules **36**, 9851 (2003).

119. J. Li, J. Jiang, C. Li, M. Y, Lin, S. A. Schwarz, M. H. Rafailovich, and J. Sokolov, Macromol. Rapid Commun. **27**, 1787 (2006)

120. M. Alexandre, G. Beyer, C. Henrist, R. Cloots, A.Rulmont, R. Jerome, Ph. Dubios, Macromol. Rapid Commun. **22**, 643 (2001)

121. H. van Olphen, An introduction to Clay colloid Chemistry,: John Wiely and Sons; New York, 1977 ; F. Pignon, A. Magnin, and J. M. Piau, Phys. Rev. Lett. **79**, 4689 (1997).

122 A. Nelson and T. Cosgrove, Langmuir **20**, 2298 (2004)

123. S. Lin-Gibson, H. Kim, G. Schmidt, C. C. Han, and E. K. Hobbie, J. Colloid Interface Sci. **274**, 515 (2004).

124. G. Schmidt, A. I. Nakatani, P. D. Butler, and C. C. Han, Macromolecules **35**, 4725 (2002).

125. M. Shibayama, T. Karino, S. Miyazaki, S. Okabe, T. Takehisa, and K. Haraguchi, Macromolecules **38**, 10772 (2005)

126. F. Perrin, J. Phys. Radium **5**, 497 (1934).

127. H. G. Jerrard, Chemical Review **59**, 345 (1959).

128. M. Doi and S. F. Edward, *The Theory of Polymer Dynamics*, Oxford University Press, 1986.

129. M. Bjorling, Macromolecules **25**, 3956 (1992).

130. W. Liang, Th. F. Tadros, P. F. Luckham, Langmuir **9**, 2077(1993)

131. J. S. Shay, S. R. Raghavan, S. A. Khan, J. Rheol. **45**, 913 (2001)

132. B. Hammouda, D. Ho, and S. Kline, Macromolecules **35**, 8578 (2002).

133. P. Debye, H. R. Anderson, and H. Brumberger, J. Appl. Phys.**28**, 679 (1957).

134. E. Loizhou, P. Butler, L. Porcar, E. Kesselman, Y. Zalman, A. Dundigalla, and G. Schmidt, Macromolecules **38,** 2047 (2005)

135. A. Dundigalla, S. Lin-Gibson, V. Ferreiro, M. M. Malwitz, and G. Schmidt, Macromol. Rapid Commun. **26**, 143 (2005)

136. N. A. Peppas, Y. Huang, M. Torres-Lugo, J. H. Ward, and J. Zhang, Annu. Rev. Biomed. Eng. **2**, 9-29 (2000)

137. A. P. Nowak, V. Breedveld, L. Pakstis, B. Ozbas, D. J. Pine, D. Pochan, T. J. Deming, Nature **417**, 424 (2002)

138. K. Haraguchi and H. Li, Macromolecules **39**, 1898(2006**)**

139. L. Harnau, D. Costa and J.-P. Hansen, Europhys. Lett. **53**, 729 (2001)

140. P. Levitz, E. P. Levitz, E. Lecolier, A. Mourchid, A. Delville, and S. Lyonnard, Europhys. Lett. **49**, 672 (2000)

141. J. Swenson, M.V. Smalley, and H. L. M. Hatharasinghe, Phys. Rev. Lett. **81**, 5840(1998)